The Dissertation Committee for Brooks Douglas Rabideau Certifies that this is the approved version of the following dissertation:

THE SELF-ASSEMBLY OF COLLOIDAL PARTICLES INTO 2D ARRAYS

Committee:

Roger T. Bonnecaze, Supervisor

Brian A. Korgel

C. Grant Willson

Thomas M. Truskett

David A. Vanden Bout

THE SELF-ASSEMBLY OF COLLOIDAL PARTICLES INTO 2D ARRAYS

by

Brooks Douglas Rabideau, B.S.

DISSERTATION

Presented to the Faculty of the Graduate School of
The University of Texas at Austin
in Partial Fulfillment
of the Requirements
for the Degree of

DOCTOR OF PHILOSOPHY

The University of Texas at Austin
December 2007

Dedication

To My Parents, Dana and Clara Rabideau

Acknowledgements

First and foremost, I would like to thank my advisor Roger Bonnecaze to whom I am deeply indebted. His years of care and dedication with me not only proved extremely helpful and insightful but taught me far more than any class could ever offer. I simply learned through watching him work; his thought process, his approach to problems, his lectures and his presentations. I simply cannot express how much he did for me. Thank you.

I am very grateful for the earlier work of Jeff Gray and Harvey Klein, whose tethered RSA simulation really helped me get started with my projects. Though it caused much heartache trying to read and understand 40 pages of complicated and, at times, cryptic code, in the long run it was of immense help to me and would serve as the foundation of my Monte Carlo simulations. Parag Shah helped point me in the right direction of a number of articles detailing relevant interparticle forces, giving me a great head start on my first project. Additionally, the elder members of the Bonnecaze group - Vatsan and Jay Norman - were of great help when encountering programming bugs. Their suggestions saved me lots of time in my futile search for them.

The basis of chapter 4 came about through the initial work of Lindsey Pell and Brian Korgel. Lindsey synthesized the a-Si particles and observed their self-organization; I was later approached to develop a simulation that would compliment the experimental observations with an explanation as to their self-organization. Though I was originally

tasked with writing the paper much of it was later reorganized and parts rewritten by Dr. Korgel. Additionally, Michel Cloitre, my office mate at the time, offered many helpful suggestions that got the simulation running.

I am also very grateful for the support from the National Science Foundation, Sandia National Laboratories, and the University of Texas at Austin Engineering Thrust 2000.

I would especially like to thank my parents. Without their years of guidance and encouragement I would probably where I am today. Thank you.

THE SELF-ASSEMBLY OF COLLOIDAL PARTICLES INTO 2D ARRAYS

Publication No._____________

Brooks Douglas Rabideau, Ph.D.
The University of Texas at Austin, 2007

Supervisor: Roger T. Bonnecaze

As the feature size of new devices continues to decrease so too does the feasibility of top-down methods of patterning them. In many cases bottom-up methods are replacing the existing methods of assembly, as having building blocks self-organize into the desired structure appears, in many cases, to be a much more advantageous route.

Self-assembled nanoparticulate films have a wide range of potential applications; high-density magnetic media, sensing arrays, meta-materials and as seeds for 3D photonic crystals to name a few. Thus, it is critical that we understand the fundamental dynamics of pattern formation on the nanoparticulate and colloidal scale so that we may have better control over the formation and final quality of these structures. We study computationally the self-organization of colloidal particles in 2D using both Monte Carlo and dynamic simulation

We present 3 studies employing Monte Carlo simulation. In the first study, Monte Carlo simulations were used to understand the experimental observation of highly-ordered 2D arrays of bidisperse, stabilized gold nanoparticles. It was shown that the LS

lattice forms with the addition of interparticle forces and a simple compressive force, revealing that bidisperse lattice formation is, in fact, a dynamic process.

It was evident that the LS lattice forms in large part because the particles within the lattice reside in their respective interparticle potential wells. In the second Monte Carlo study, this information was used to predict size-ratios and surface coverages for novel lattice structures. These predictions are intended to guide experimentalists in their search for these exciting new structures.

In the third study it was shown that polydisperse amounts of amorphous-silicon nanoparticles could form 2D clusters exhibiting long-range orientational order even in the absence of translational order. Monte Carlo simulations were performed, which included lateral capillary forces and a simple stabilizing repulsion, resulting in structures that were strikingly similar to the experimentally observed

In the fourth study we used dynamic simulation to study the hydrodynamically-assisted self-organization of DNA-functionalized colloids in 2D. It was shown that hydrodynamic forces allow a more thorough sampling of phase space than through thermal or Brownian forces alone.

Table of Contents

List of Tables

List of Figures

Chapter 1. Introduction

As the feature size of new devices continues to decrease so too does the feasibility of top-down methods of patterning them. Photolithographic techniques, for example, have managed to produce smaller and smaller features, coping with many of the predicted limits. These new and innovative techniques however, side-step impending difficulties yet bring with them their own set of challenges. For example, a technique that replaces the usual air gap between the lens and the wafer with a liquid medium – known as immersion lithography - can substantially enhance resolution but leads to new issues such as air entrainment and watermarks which are left to be resolved. Additionally, the costs associated with the implementation of these new techniques can be quite considerable.

In many cases bottom-up methods are replacing the existing methods of patterning, as having building blocks self-organize into the desired structure appears, in many cases, to be a much more advantageous route. In fact, this is the method nature employs - and with amazing success. Fiery opals, intricate snowflakes, the iridescent glow of butterfly wings and even the elaborate spiral of a nautilus shell; all are formed without the direction of an outside source. In each case the resulting structure is the product of self-organization. Even more amazing is the complexity and precision with which biological systems operate. The development of a fully grown, highly functional organism from just a single cell is a marvelous occurrence; even more awe-inspiring is the fact that the organism self-organizes under the sole supervision of just one set of directions. It is no coincidence that this approach, having building blocks self-organize into the desired structure, garners such immense interest; the possibilities are extraordinarily vast and almost inconceivably far-reaching. To mimic nature, however, we must first understand the fundamentals of self-organization.

Self-assembled nanoparticulate and colloidal films have gathered a lot of interest in the past few years and with good reason; these films have a wide range of potential application in such things as high-density magnetic media, 2D sensor arrays, photonic devices and as the next generation of hybrid metamaterials.

As we enter into the digital age we are left with the task of manipulating and storing enormous amounts of data. We are surrounded by colossal amounts of data. Entire digital photo albums, audio and video libraries, even encyclopedias; more and more things are being stored in digital formats these days and even the formats themselves grow larger (e.g. the recent conversion to hi-definition). Combine this with the recent trend - making devices highly portable (e.g. smaller laptops, portable MP3 players, camera phones, etc…) - and data storage becomes an issue of great importance. Current work has focused on monolayers of self-assembled ferromagnetic nanoparticles for use as high-density magnetic media. This new device has the stunning capability of storing terabytes of information per square inch of material. Any defects in the recording medium, however, have the potential to disrupt the read/write process - making it essential that we understand the process of monolayer formation and can maintain a high degree of order throughout the entire structure.

Colloidal monolayers have another application in the field of 2D sensor arrays. Possible uses for these arrays include probing samples for specified biochemicals, detecting minute light sources and sensing extremely small electromagnetic disturbances. These, of course, are just a few of the many possibilities. As miniature devices, including the celebrated lab-on-a-chip device, become more and more commonplace the demand for defect free 2D sensor arrays should grow considerably.

Another field that could greatly benefit from self-assembled nanoparticulate films is the area of photonic devices - devices with the ability to control and manipulate the flow of light in new and exciting ways. It has even been speculated that these devices might one day spawn a new field of optical computing. Two-dimensional nanoparticulate monolayers will serve as the seeds for the growth of 3D photonic devices. It is thus crucial that we maintain high-fidelity in the 2D seeds as the photonic band gaps are highly sensitive to the periodicity of the structure. Any defects or irregularities could prove highly detrimental to the functionality of the resulting photonic crystal.

One last example of the potential application of nanoparticulate films is as metamaterials – new hybrid materials with mixed optical, mechanical, and electromagnetic properties. By incorporating nanoparticles of differing materials into a periodic lattice structure it is possible to create a hybrid material with blended properties of each of the constituent materials. With this application comes the ability to custom tailor new materials for specific applications.

The above applications all illustrate just how crucial it is that we understand the fundamental dynamics of pattern formation on the nanoparticulate and colloidal scale. The goal of this thesis is to develop a fundamental understanding of the self-assembly of monolayer films of bidisperse particles.

In a previous study Doty *et. al.*[1] used Monte Carlo simulations of bidisperse hard disks to study the experimental observation of highly-ordered 2D arrays of bidisperse, stabilized gold nanoparticles. It was found, however, was that kinetic limitations prevented the formation of these structures with hard disks alone. In chapter 2 we show that the addition of interparticle forces along with a simple compression leads to the formation of 2D LS lattices; the main finding of the study being that the assembly of these lattice structures is a dynamic process. This study also yielded much insight into why the specific size-ratio favored the formation a square LS lattice. It was found that the large-large particles were aligning in their interparticle potential wells as well as the large-small particles.

It was then realized that by varying the size-ratio of the particles one could alter the potential well distances and thus the favored unit lattice structure. In chapter 3 this scheme is extended, predicting size-ratios and surface coverages favoring the formation of novel 2D bidisperse arrays. It is intended as a guide for experimentalists when searching for these exciting new structures. Melting simulations were also performed, determining whether these structures are indeed stable lattice or just short-lived metastable states.

A common belief is that the polydispersity of particles in nanoparticulate films disrupts the ordering of these systems. In fact, earlier studies by Gray *et. al.*[2] showed that this is the case for tethered hard disks that undergo random sequential adsorption. Experiments performed by L. E. Pell and B. A. Korgel, however, showed the formation of structures composed of polydisperse amorphous silica colloids exhibiting long-range orientational order – even in the absence of translational order! In chapter 4 we show just how lateral capillary forces can bring about this ordering and size-segregation in these intriguing structures.

In chapter 5 we follow the role of hydrodynamic shear as a new method for sampling phase space for DNA-functionalized colloidal particles confined to the interface of two fluids. We show that hydrodynamic assistance offers a new tool for sampling phase space in instances where thermal and Brownian forces fall short.

Together, these studies are modest steps toward a complete understanding of the self-organization of colloidal and nanoparticulate films. In instances they reveal specific insights into the process of pattern formation; in other instances they act as a guide, showing others where to look and which directions offer the best possibilities. In all, this knowledge will lead us toward a greater degree of control when creating devices of tomorrow.

It should be noted that the individual chapters of this dissertation are separate papers, each appearing in the publication *Langmuir*. The reader should be aware that there are minor amounts of reiteration throughout the chapters since each paper has been reproduced in its original form.

Chapter 2. A Computational Study of the Self-Organization of Bidisperse Nanoparticles

2.1 SUMMARY

We study computationally the self-organization of bidisperse mixtures of thiol-stabilized gold particles in two dimensions through random sequential adsorption (RSA) coupled with the Metropolis algorithm for determining surface diffusion. It was previously shown [Doty et al., Phys. Rev. E, **65**, 061503 (2002)] that ordered lattices of bidisperse particles cannot form with hard sphere interactions. Here we include the effects of interparticle forces. Osmotic and steric interactions provide a repulsive force at close distances while at longer ranges the van der Waals interaction leads to attraction. Two size-ratios (σ) of 0.375 and 0.577, determined experimentally to form LS (the two-dimensional NaCl analogue) and LS_2 (the two-dimensional AlB_2 analogue) lattices, were studied. The calculated jamming limits for RSA fall well below the minimum surface coverage necessary for stable ordering as determined by melting simulations. Uniform compression of the particles' positions, as a model of the convection and lateral capillary forces that would be experienced during solvent evaporation, allowed this critical surface coverage to be achieved and LS lattice formation was observed for $\sigma = 0.375$. No LS_2 lattice formation was observed for $\sigma = 0.577$ with compression. The melting coverage of the LS_2 lattice far exceeds the coverage observed experimentally and so is not observed.

2.2 INTRODUCTION

The production of extremely small structures, beneath the limits of modern-day lithographic techniques, is an area of intense interest these days. Self-Assembly or "bottom up" methods of manufacture are being explored as an alternative means for forming nanoscopic structures as opposed to "top down" direct patterning methodologies. Ordered patterns of nanoparticles could be used directly, for example, as high density magnetic media, if the particle were ferromagnetic, or indirectly as templating agents. Here we are particularly interested in experiments performed by Kiely *et al.*[3, 4] showing that thiol-stabilized gold particles with distinct bimodal size distributions spontaneously order into two-dimensional superlattices.

It is well known that some mixtures of bidisperse hard-spheres organize into three-dimensional superlattices driven entirely by the entropic gain[5], and it has been speculated that the same was true for the two-dimensional lattices[6]. In fact geometric packing calculations for stoichiometric lattices[7] support these speculations. Previously, numerical simulations of the random sequential adsorption (RSA) process were performed for the case of hard disks with well-defined bimodal size distributions[1] and ordered bidisperse structures were not observed for any of the RSA simulations regardless of the size ratio. The key finding was that the calculated jamming limits fell well below the minimum surface coverage necessary for stable ordering, as determined by melting simulations. Furthermore, the surface coverage at melting was well above that observed experimentally. With the results of the simulation casting doubt on the sole role of entropy for the formation of two-dimensional superlattices, this once again led us to the question of how and why do these structures form.

We speculated that interparticle forces might play a significant role in the formation of such structures. Consequently, we added van der Waals, osmotic, and steric interactions to the RSA simulation. As two colloidal particles approach one another, they first begin to feel the van der Waals attraction between the two gold cores. Upon further approach, the dodecane-thiol ligands of the particles begin to overlap, displacing a certain fraction of the intervening solvent. This creates an osmotic pressure gradient between the two particles and results in strong repulsion. At very small interparticle separations, the ligands themselves repel each other and are the reason for the addition of steric interaction. This model of the interactions is consistent with recent x-ray scattering measurements by Saunders and Korgel[8]. In addition the ratio of the radii of small to large particles reported by Kiely *et al*.[3, 4] were used as the basis for our simulations. We wondered if these interparticle interactions, naturally experienced by ligand-stabilized particles, would give rise to the experimentally observed bidisperse superlattices.

Initially, our studies began with the RSA process. Again though, it became apparent that the RSA process alone would not allow our systems to achieve the experimentally observed surface coverages. Further investigation led to the development of two additional simulations. The first is a melting simulation which, allowing the particles on an initially perfect lattice to diffuse, determines the minimum surface coverage for the stability of ordered bidisperse lattices. The other is a compression simulation which increases the surface coverage by decreasing the periodic boundary size during particle diffusion and compresses the particles' positions, forcing the system to achieve a desired surface coverage. The isotropic compression is a simple model of the concentration of particles due to evaporation-driven flow[9] and lateral capillary forces.

The remainder of the paper is divided into three sections. In the first section we examine the details of each of the three different simulations. The second section contains the results of our simulations. First, we present our results for the LS lattice for the RSA, melting, and compression simulations. We then present the results of the same simulations for the LS_2 lattice; it will be seen that the behavior for this lattice is quite different from the LS lattice. In the final section we conclude with a discussion of the results.

2.3 SIMULATIONS

We employed three different simulations in our study: an RSA simulation, a melting simulation, and a compression simulation. The RSA simulations have been described in detail earlier[2, 10] Briefly, colloidal particles are adsorbed to the surface following the standard RSA procedure of placing particles at random locations in a periodically replicated square and rejecting overlapping particle placements and placements of unfavorable energetic change. Formation of the LS and LS_2 lattices requires that a specific ratio of small to large particles is present in the system. Therefore, particle adsorption for RSA follows in such a way that the ratio of the surface number fractions (n_S / n_L) is maintained. This is accomplished by choosing a particle for adsorption such that its successful attachment to the surface will on average satisfy the number fractions required by the L_mS_n array of interest. Particles diffuse on the surface between adsorption attempts according to the Metropolis algorithm, adjusting the step size to obtain 50% acceptance of moves[11]. The magnitude and direction of each move are selected from two uniform distributions. Moves that lead to overlap of the particles hard cores or which are deemed unacceptable energetically by the Metropolis algorithm are rejected. Typically, two hundred Metropolis cycles are completed after every successful adsorption attempt, where a cycle is defined as N successful moves, with N as the current number of adsorbed particles. Since most particle adsorption attempts are unsuccessful (10^{-8} success rate at long times), surface diffusion far exceeds particle addition rates at long times when the important phase behavior and kinetics are observed. Despite many attempts, including the modification of the relative magnitude of the interparticle potentials, the RSA simulations do not form stable LS or LS_2 lattices. This then led us to our melting simulation. Melting simulations are performed by replicating a perfect L_mS_n lattice and allowing the particles to diffuse according to the Metropolis Algorithm. Simulations were performed for the LS and LS_2 lattices comprised of large and small colloidal particles with the appropriate size ratios, $\sigma = 0.577$ (LS_2) and $\sigma = 0.375$ (LS), taken from previous experimental observtions[1,2]. For the purposes of this paper $\sigma = R_L / R_S$, where R_S and R_L are the radii of the small and large particles, respectively. The particles are allowed to diffuse for one million cycles and the results are visually examined. A lattice is regarded as having melted if the particles stray well beyond their mean lattice positions. In practice it is very obvious to tell whether or not a structure has melted. If the structure did melt, the interparticle spacing is decreased or conversely the coverage is increased and the process is repeated. Typically, melting occurs in the first few thousand diffusion cycles, but near the melting coverage it takes considerably more diffusion cycles and is sometimes difficult to tell if melting will ever occur. We considered lattices that remained stable after five million diffusion cycles as stable structures.

As will be seen from the results of the melting simulations, it was apparent that the surfaces could not attain high enough coverages to form stable structures with RSA alone. To attain the desired surface coverages we employed a compression simulation.

The compression simulations are performed by decreasing the periodic boundary box size by a factor of one ten-thousandth and performing a uniform compression of all of the particles positions every two hundred diffusion cycles. This rather large number of diffusion cycles when compared to the compression factor, gives the particles enough time to adjust their position and re-equilibrate before the next compression step is performed.

Due to the extremely large number of energetic calculations required for all the simulations, the process was sped-up with the creation of a look-up table used in all the simulations. In addition, the overlap and energetic calculations were implemented using a grid of 16 cells to accelerate the computation. By dividing the simulation box into cells, only those cells in the vicinity of the particle of interest need to be investigated for energetic calculations and particle overlap. Typical RSA simulations would run for 24 hours on a Dell UNIX workstation. Melting simulation times were highly dependent on the surface coverage, *i.e.*, low surface coverages melted after only a few minutes of simulation time or less than 1000 diffusion attempts, while others remained stable after 24 hours of simulation time or diffusion attempts on the order of 10^6. Compression simulations required the most time, as expected by the large diffusion time between compressions and were generally run for 48 to 72 hours.

The Interparticle Potentials

The interparticle potentials included in the simulations were van der Waals attraction along with osmotic and steric repulsions of the form proposed by Vincent et al. For simplicity, all potentials have been non-dimensionalized by thermal energy, *kT*, where k is the Boltzmann constant and T is the temperature of the system.

The van der Waals potential for two spheres of unequal radii r_i and r_j at a dimensionless center-to-center distance d is given by[12]

$$V_A(d) = -\alpha\left[\frac{2}{\left(s^2-4\right)} + \frac{2}{s^2} + log\left(\frac{s^2-4}{s^2}\right)\right], \qquad (1)$$

where $s^2 = 2d / (r_i + r_j)$ and the dimensionless parameter $\alpha = A_{12321} / (6kT)$. A_{12321} is the overall Hamaker constant through the gold, dodecane-thiol, and toluene layers and a value of 0.931 eV was used. A value of $\alpha = 6.04$ corresponding to $T = 298$ K was used for all the simulations.

The osmotic and steric potential used in the simulations proposed by Vincent *et al.*[13] are given by

$$V_{osm}(d) = \beta\left(\varphi\left(d\right)\right)^2 a\left(\delta - \frac{\left(d-2a\right)}{2}\right)^2 \qquad \delta < d - 2a < 2\delta, \qquad (2)$$

$$V_{osm}(d) = \beta\left(\varphi\left(d\right)\right)^2 a\delta^2\left(\frac{\left(d-2a\right)}{2\delta} - \frac{1}{4} - log\left(\frac{\left(d-2a\right)}{\delta}\right)\right) \qquad 0 < d - 2a < \delta \qquad (3)$$

$$V_{elas}\left(d\right) = \gamma\varphi\left(d\right)a\delta^2\left\{\frac{\left(d-2a\right)}{\delta}log\left[\frac{\left(d-2a\right)}{\delta}\left(\frac{3-\frac{\left(d-2a\right)}{\delta}}{2}\right)^2\right] - log\left(\frac{3-\frac{\left(d-2a\right)}{\delta}}{2}\right) + 3\left(1-\frac{\left(d-2a\right)}{\delta}\right)\right\}$$

$$0 < d - 2a < \delta, \qquad (4)$$

where the two dimensionless parameters are given by $\beta = 4\pi R^3 / \upsilon_1$ and$\gamma = 2\pi R^3\rho / M_w$. The parameter υ_1 is the molecular volume of the solvent, $\phi(d)$ is the effective volume fraction of polymer in the adjacent layer, χ is the Flory-Huggins solvency parameter for the polymer, M_w is the molecular weight of the stabilizing moiety, and ρ is its density.

Here R is the dimensional radius of the large particle, a is the dimensionless radius of the particle (if the interaction was between a large and a small particle the average of the two was used), and δ is the dimensionless thickness of the adsorbed polymer layer. The values used in the simulation are as follows: $\upsilon_l = 1.77\times10^{-28}$ m^3, $\chi = 0.3$, $M_w = 3.35\times10^{-22}$ g/molecule, $\rho = 0.866$ kg/L, $R = 4.0$ nm, $\delta = 0.187$. The resulting values of β and γ are 36 000 and 8 320, respectively. The volume fraction of ligand $\varphi(d)$ is given by

$$\varphi(d) = \frac{N_{ligand} A_{ligand}}{R^2 d^2}, \tag{5}$$

where N_{ligand} is the number of ligand molecules attached to the metallic core and A_{ligand} is the cross-sectional area of the ligand molecule. Values of these parameters used in the simulation are: $N_{ligand} = 1195$ (large particle), $N_{ligand} = 398$ (small particle), and $A_{ligand} = 1.45\times10^{-19}$ m^2. For interactions between large and small particles an average of the ligand volume fraction was used.

A hard-sphere cutoff limit was chosen as the interparticle spacing corresponding to the maximum of the interparticle potential (typically above 75 kT) and any sampling closer than this limit resulted in rejection. This not only served to exclude inaccessible phase space, but also aided in slight acceleration of the simulation. Figure 2.1 illustrates the interparticle potential for $\sigma = 0.375$. It should also be noted that our model for the interparticle potential is in good agreement with the recent findings of Saunders and Korgel[7], both qualitatively and quantitatively.

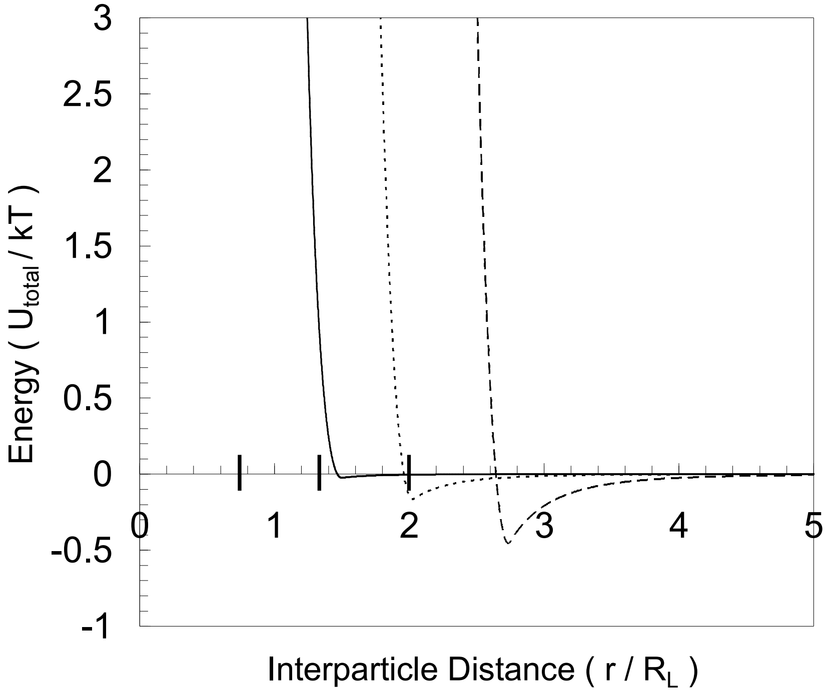

Figure 2.1: The interparticle potential for $\sigma = 0.375$ between two large particles (dashed-line), a large and a small particle (dotted-line), and two small particles (solid-line) using $\alpha = 6.04$, $\beta = 36\,400$, and $\gamma = 8\,320$. Large bars on the x-axis indicate the hard sphere contact distance for the small-small, large-small, and the large-large respectively.

There are three distinct potential curves corresponding to the interactions between two large particles, two small particles, and a large and a small particle. The large-large potential has the deepest well, a direct result of increased van der Waals attraction due to larger metallic cores. Likewise, the small-small potential has a much shallower well because it has less polarizable gold. As mentioned before, three dimensionless groups dominate this problem. The first α is a ratio of the energy due to the van der Waals interaction and the thermal energy in the system. The second dimensionless group β relates the osmotic energy with the thermal energy of the system. And the third dimensionless number γ relates the elastic energy with the thermal energy of the system. By tuning the values of these parameters we are able to tune the amount of thermal energy in the system. Varying the parameters by reasonable amounts had little effect on the observed results.

2.4 RESULTS

The LS Lattice ($\sigma = 0.375$)

Figure 2.2 shows representative images of the resulting structures obtained from the RSA simulation for the LS lattice for increasing time. The surface coverage of particles increases with time and the interparticle forces clearly influence the mean particle spacing.

Stable LS structures, however, were not observed for RSA simulations with $\sigma = 0.375$. Many different attempts were made towards improving the resulting structures from the RSA. The dimensionless groups of the problem were varied, in effect raising and lowering the thermal energy of the system, but no noticeable changes were observed. The pairwise radial distribution functions were computed on the resulting RSA structures (not shown here) confirming what was observed by the eye, namely a disordered, two-dimensional liquid-like state.

Kinetic data from the RSA simulations for the size ratios $\sigma = 0.375$ and $\sigma = 0.577$ with stoichiometry corresponding to the LS and LS_2 lattices, respectively, are shown in Figure 2.3.

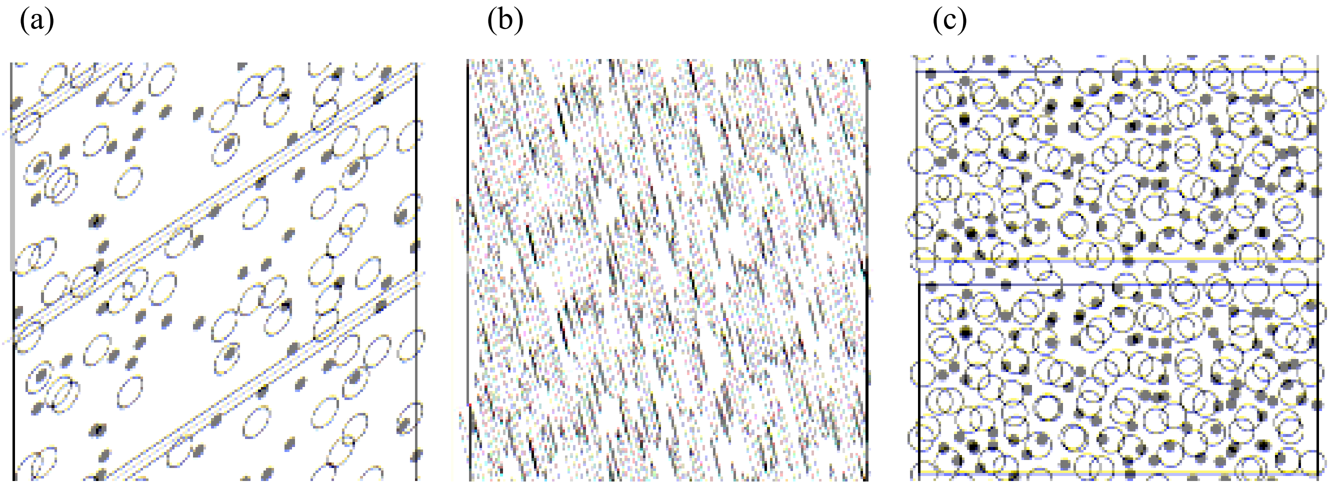

Figure 2.2: Surface evolution during RSA for $\sigma = 0.375$ for (a) $N = 64$ and $\theta = 0.127$, (b) $N = 128$ and $\theta = 0.255$ and (c) $N = 192$ and $\theta = 0.382$. $\alpha = 6.04$, $\beta = 36\ 400$, $\gamma = 8\ 320$.

The kinetic data can be plotted in an alternate power law form (generalizing the form conjectured by Feder[14] and derived by Pomeau[15] and Swendsen[16]):

$$\theta = \theta_\infty - c\left(\frac{na}{A}\right)^{-b} , \tag{6}$$

where θ is the fractional areal coverage on the surface and n is the number of adsorption attempts normalized by the area of the simulation cell A, and the disk area a, to obtain the jamming limit coverages θ_∞, and the two kinetic parameters, c and b. The parameters were fit using the Levenberg-Marquardt algorithm. For $\sigma = 0.375$ and $n_S/n_L = 1$ it was found that $\theta_\infty = 0.406$, $c = 0.190$, and $b = 0.195$. For the $\sigma = 0.577$ and $n_S/n_L = 2$ it was found that $\theta_\infty = 0.394$, $c = 0.208$, and $b = 0.194$. For both cases the jamming limit coverages fell well short of their respective coverages required for stability of the lattice. The power law exponent b for the two cases differs from the classic (monodisperse) RSA result of 1/2. We attribute this to the bidispersity of the suspension. Previous studies have in fact shown that increases in the polydispersity lead to slower adsorption kinetics.[2, 17-19] In addition, rejection of adsorption attempts leading to unfavorable energetic interactions may also retard the adsorption rate.

Because the RSA simulation was unsuccessful with forming a stable LS lattice, melting simulations (or simulations of stability) were performed to determine the lower bounds on the coverage θ for maintaining stable LS lattices. It was determined that a surface coverage that is greater than 0.445 is necessary to maintain an ordered LS array. Figure 2.4 shows the stability of an LS lattice with $\sigma = 0.375$ at the experimentally determined surface coverage $\sigma = 0.470$ [1,2].

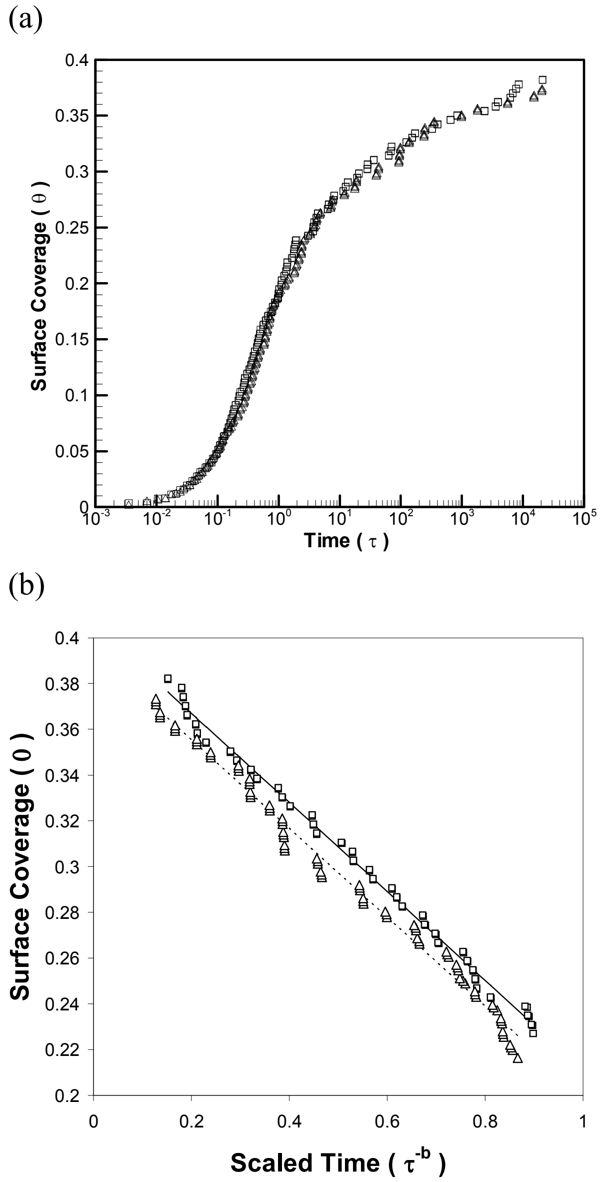

Figure 2.3: Kinetic results of RSA simulation showing (a) coverage versus time ($\tau = na/A$) and (b) coverage vs. scaled time (τ^{-b}): (□)$\sigma = 0.375$, (Δ) $\sigma = 0.577$, (Δ) $\sigma = 0.577$; $\alpha = 6.04$, $\beta = 36\ 400$, $\gamma = 8\ 320$.

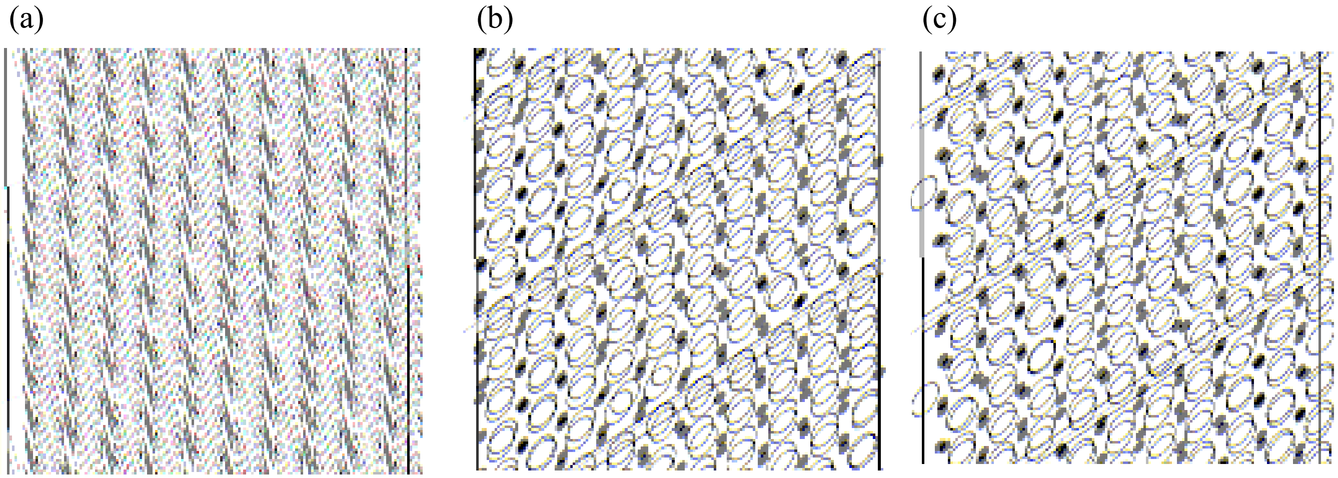

Figure 2.4: Stability of an LS lattice with $\sigma = 0.375$ and $\theta = 0.470$ after (a) zero, (b) 2 000 000, and (c) 4 000 000 diffusion cycles. $\alpha = 6.04$, $\beta = 36\ 400$, $\gamma = 8\ 320$.

The Helmholtz free energy relative to a reference state, *F-Fr*, of a perfect LS lattice was calculated for different surface coverages and the results are shown in figure 2.5. The plot shows that at low surface coverages (large interparticle distances), the free energy decreases with increasing coverage, corresponding to the attractive van der Waals interaction at this distance. As the surface coverage increases (short interparticle distance), however, the repulsive component of the potential begins to dominate, increasing the free energy with increasing coverage. Thus, there is a minimum in the free energy of the LS lattice.

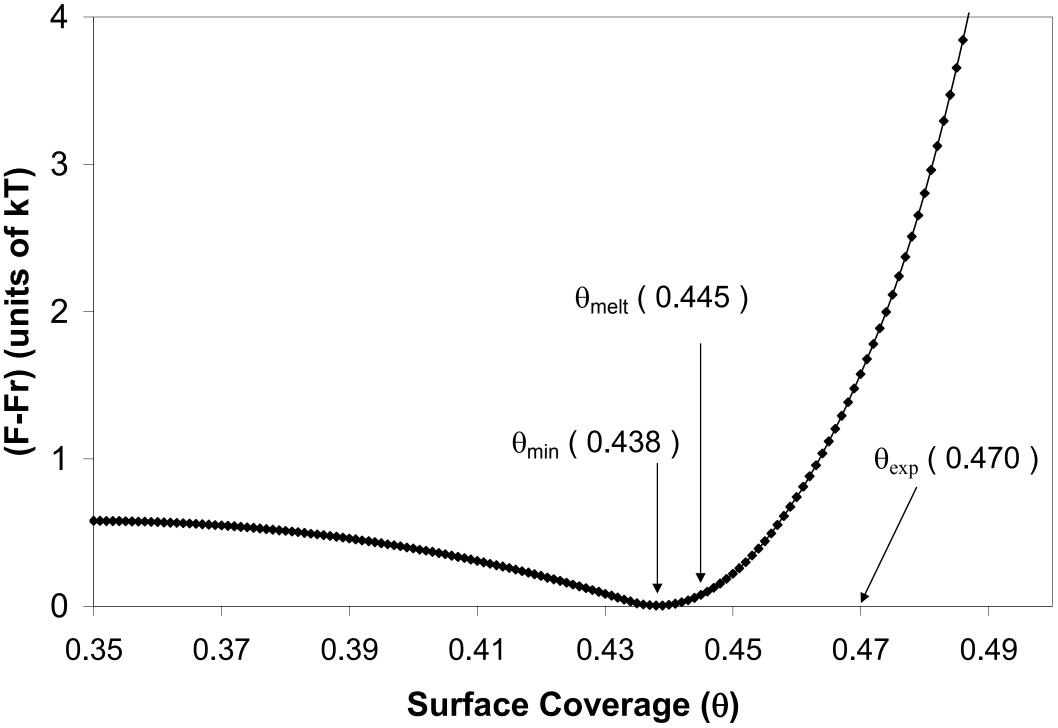

Figure 2.5: The Helmholtz free energy per unit cell (consisting of two particles) of a perfect LS lattice. "θ_{min}" denotes this plot's minimum value, "θ_{melt}" denotes the minimum surface coverage required for stability as determined by the simulation, and "θ_{exp}" denotes the surface coverage of Kiely's experimental photographs. $\alpha = 6.04$, $\beta = 36\ 400$, $\gamma = 8\ 320$.

Also included in the plot are the locations of the minimum surface coverage required for stability along with the surface coverage determined from Kiely's experiments. Notice that the melting coverage is slightly above the coverage at the minimum of the free energy, both of which are well below the experimental coverage. The experimentally observed coverage does not correspond to coverage at the lowest theoretical free energy for the two-dimensional crystal. This may indicate that the experimentally observed system is not an equilibrium configuration.

The melting coverage of $\theta = 0.445$ is well above the jamming limit coverage of $\theta_\infty = 0.406$ obtained from the RSA simulation. It is thus apparent that ordered LS lattice cannot be achieved in two-dimensions by the RSA process alone. Some other factor must be responsible for driving the system above the required surface coverage for stability (e.g., lateral capillary forces and/or evaporation). A simple method for achieving the desired surface coverage was devised by uniform compression of the particles' positions between diffusion cycles while decreasing the periodic boundary box size. Compression simulations were implemented on the fully developed RSA structures, forcing each system to achieve their necessary surface coverage. Figure 2.6 shows three snapshots of the evolution of the structure for $\sigma = 0.375$ and stoichiometry for an LS lattice particulate system during the compression simulation. On inspection an LS lattice can be seen in the middle-right section of Figure 2.6(c), as highlighted.

To determine whether or not the lattice formation was aided by the small system size, the size of the periodic square was quadrupled and the RSA and compression simulations were repeated. Figure 2.7 shows the resulting structure.

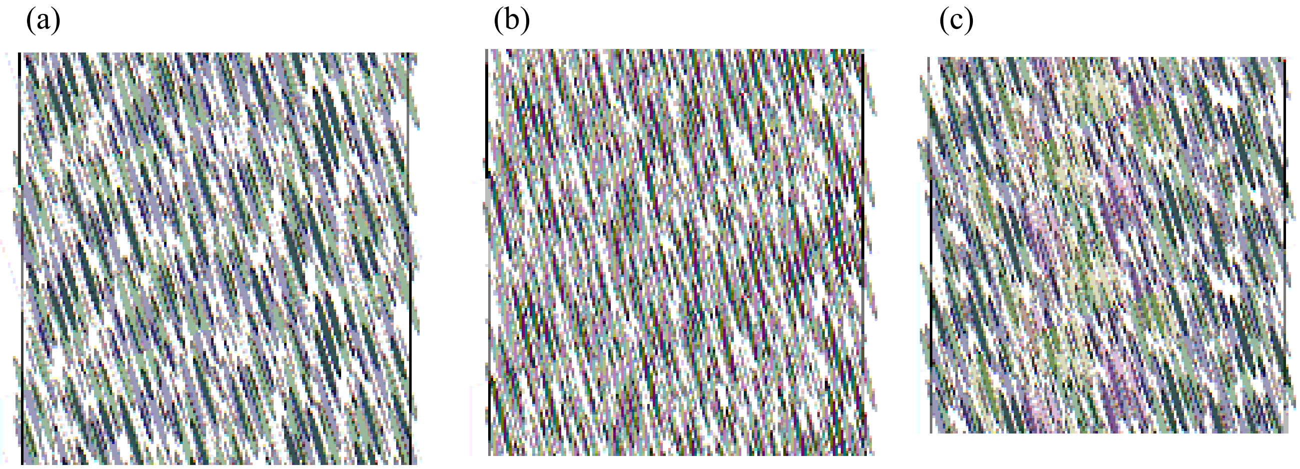

Figure 2.6: Unilateral compression for $\sigma = 0.375$. (a) $\theta = 0.409$, (b) $\theta = 0.439$, and (c) $\theta = 0.470$ (Kiely's θ). $\alpha = 6.04$, $\beta = 36\,400$, $\gamma = 8\,320$.

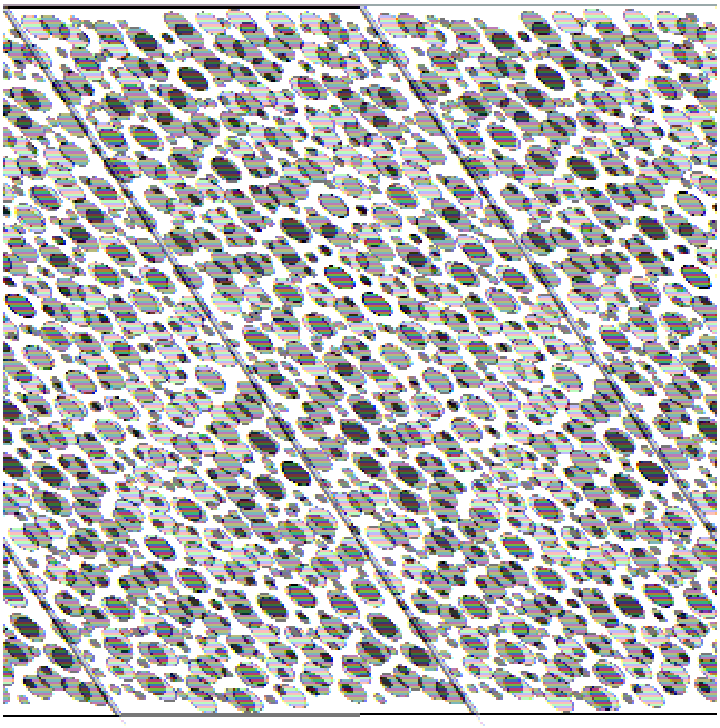

Figure 2.7: Resulting structure at $\theta = \theta_{exp} = 0.470$ of the compression simulation with quadruple the number of particles for $\sigma = 0.375$. $\alpha = 6.04$, $\beta = 36\ 400$, $\gamma = 8\ 320$.

A number of individual lattices can be seen highlighted in yellow. The lattice appears to form because of the geometrical relation of the locations of the respective large-large and large-small potential minimums. Specifically, the center to center distance corresponding to the large-small potential minimum is the hypotenuse distance of a triangle whose legs are half of the center to center distance corresponding to the large-large potential minimum. When the particles align in such a way as to form this LS lattice the large-large and large-small potentials are each in their respective minimums. The potential minimum of small-small particles is inconsequentially small.

The LS$_2$ Lattice ($\sigma = 0.577$)

Stable LS$_2$ structures were not observed for RSA simulations for $\sigma = 0.577$. The jamming limit coverage (θ_∞) obtained by the RSA simulations was 0.394. Figure 2.8 shows representative images of the resulting random structures obtained in the RSA simulation.

From the melting simulations for $\sigma = 0.577$, the minimum surface concentration necessary for stable ordering into an LS$_2$ lattice was found to be $\theta = 0.809$. This surface coverage corresponds to the maximum packing of an LS$_2$ lattice as allowed by the hard-sphere cutoff limits. In addition, no restoring force, like that seen for the LS lattice, was observed. For this size ratio as well, θ_∞ fell far below the values of surface coverage required for stability. Figure 2.9 shows the instability of an LS$_2$ lattice at the experimentally observed surface coverage θ_{exp}=0.549.

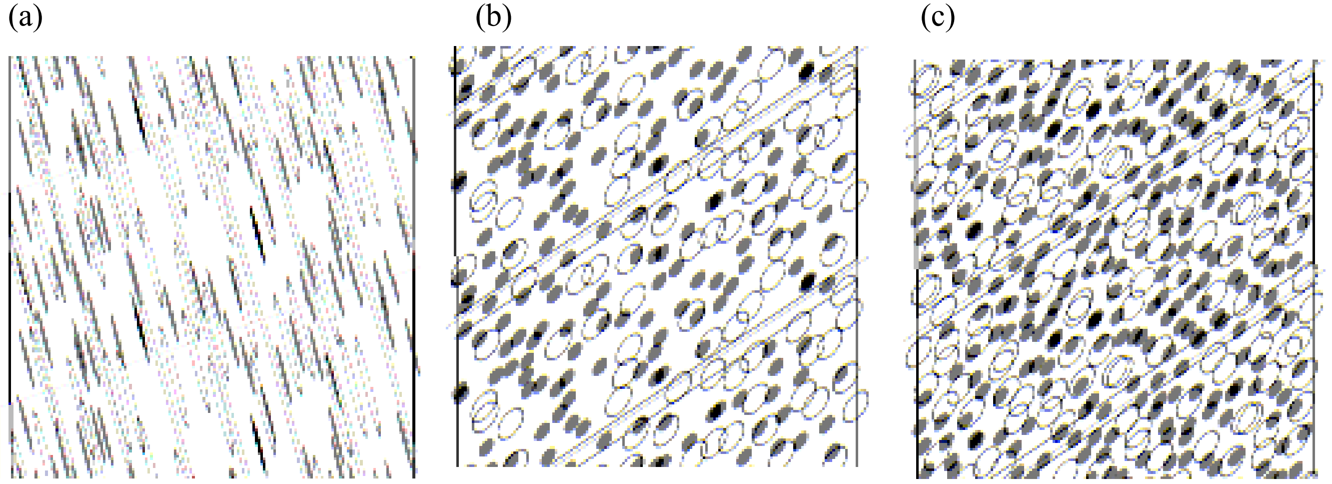

Figure 2.8: Surface evolution during RSA with $\sigma = 0.577$ for (a) $N = 64$ and $\theta = 0.123$, (b) $N = 128$ and $\theta = 0.249$ and (c) $N = 193$ and $\theta = 0.373$. $\alpha = 6.04$, $\beta = 36\,400$, $\gamma = 8\,320$.

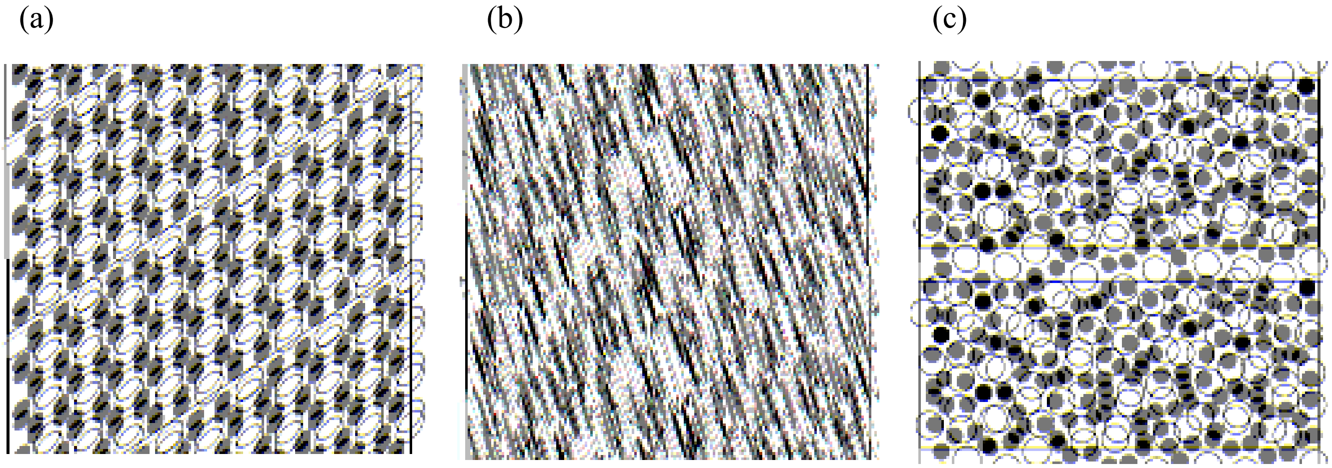

Figure 2.9: Instability of an LS$_2$ lattice with $\sigma = 0.577$ and $\theta = 0.549$ after (a) zero, (b) 2 000 and (c) 10 000 diffusion cycles. $\alpha = 6.04$, $\beta = 36\ 400$, $\gamma = 8\ 320$.

Notice that after only a few thousand diffusion cycles the particles associate into strands of like particles. This is due largely in part to the fact that the potential minimums of the large-large and small-small interactions occur at an interparticle distance that is much closer than that of the perfect LS_2 lattice. Any perturbation to the system allows particles that are alike to move closer together towards their potential minimum interparticle distance and hence leads to the formation of strands of like particles.

The Helmholtz free energy of a perfect LS_2 lattice was calculated like that of the previously described LS lattice and the results shown in Figure 2.10.

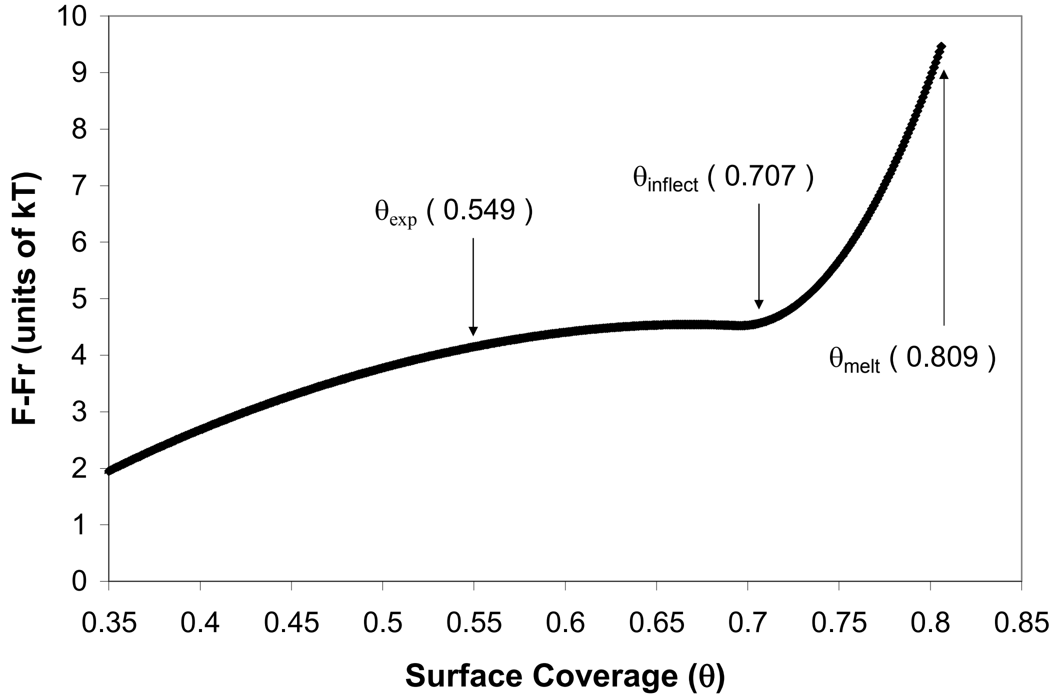

Figure 2.10: The Helmholtz free energy per unit cell (consisting of three particles) of a perfect LS_2 lattice. "$\theta_{inflect}$" denotes this plot's inflection point, "θ_{melt}" denotes the minimum surface coverage required for stability as determined by the simulation, and "θ_{exp}" denotes the surface coverage of Kiely's experimental photographs. $\alpha = 6.04$, $\beta = 36\,400$, $\gamma = 8\,320$.

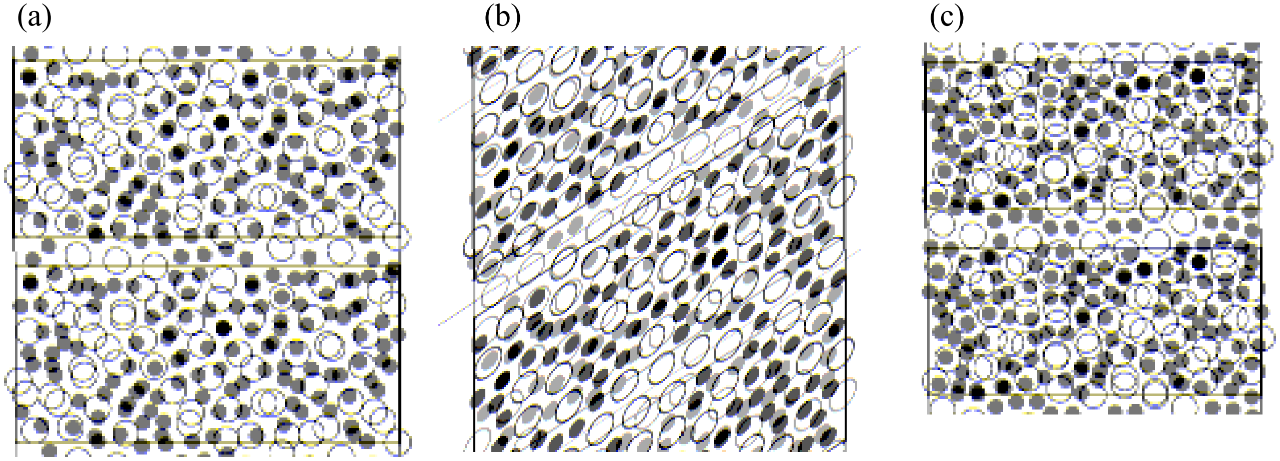

Figure 2.11: Uniform compression for $\sigma = 0.375$. (a) $\theta = 0.424$, (b) $\theta = 0.483$, and (c) $\theta = 0.549$ (Kiely's θ). $\alpha = 6.04$, $\beta = 36\ 400$, $\gamma = 8\ 320$.

In this case there is not a local minimum in the free-energy like that of the LS lattice, but rather an inflection point. Notice that the required surface coverage for stability is far beyond both the coverage corresponding to the plot's inflection point and the experimental surface coverage.

Figure 2.11 shows the evolution of the $\sigma = 0.577$ particulate system throughout the compression simulation. It is seen that the resulting system, Figure 2.11 (c), shows little resemblance to the experimentally observed LS_2 structure.

2.5 DISCUSSION

We did not see the formation of LS lattices in the RSA simulations even with the addition of interparticle forces. Based on our melting simulation results, RSA is not able to attain a high enough surface coverage to achieve stability. However, by compressing the resulting structures from the RSA simulations beyond their melting coverage, we did see the formation of a number of rafts of LS lattices. The additions of the interparticle forces and compression are crucial to the formation of stable LS lattices.

In much the same way, stable LS_2 lattices did not form with the RSA simulations and the addition of interparticle forces. High enough surface coverage could not be attained for stability as determined by the melting simulations. Unlike the LS lattice, however, stable LS_2 lattices did not form when the system was compressed to the experimental surface coverage. This is due to the fact that other than at closest packing, the forces between like particles always causes them into contact disrupting the LS_2 lattice.

Based on the instability of the LS_2 melting simulation results at the experimentally observed surface coverage it was obvious that the LS_2 structure had little chance of formation with our choice of interparticle potentials. There must be another factor responsible for the stability of the LS_2 lattice at the experimental conditions which might also contribute to its formation.

The capillary immersion force was considered as a means to resolve the above-mentioned problem. These lateral capillary forces were approximated with pairwise interaction potentials[20] assuming that the particles are perfectly wetting. However, when added to the simulations, these new interparticle forces proved not to be a factor in the lowering of the melting point for the LS_2 lattice. The only way for this problem to be alleviated is to further extend the repulsive forces between small particles. Therefore, the addition of the capillary immersion force is of no help. The nanoparticles are in fact faceted, and one possible speculation is that interactions between facets may stabilize the LS_2 lattice at lower coverages.

Lateral capillary forces do in fact give rise to a compression of the particles when the film thickness becomes comparable to the particle diameters.[21] It has been seen in experiments using polydisperse particles that as the film thickness decreases the largest particles form the nucleus of the clump and the particle sizes decrease the further from the nucleus they are.[22] In the end, we used a simple but representative model of these complex lateral capillary forces through our compression simulation. The compression was necessary to achieve the experimentally observed coverages and for the formation of an ordered structure in the case of the LS lattice.

The self-assembly of these bidisperse structures is a non-equilibrium process. The dynamics of the process are crucial in the formation of these lattices. Essentially, it is necessary to include the interparticle forces along with compression to observe the formation of these bidisperse lattices. Additionally, it appears other forces must be taken into account for the formation of the LS_2 structures.

Chapter 3. Computational Predictions of Stable 2D Arrays of Bidisperse Particles

3.1 SUMMARY

We study computationally the stability of various 2D arrays of bidisperse mixtures of stabilized nanoparticles through a melting simulation employing the Metropolis algorithm for determining surface diffusion. In our previous work [Langmuir 2004, 20(21), 9408] we studied computationally the stability of bidispersed, monolayers of thiol-stabilized gold nanoparticles with a size ratio (σ) of 0.375. We found that interparticle forces were essential to stabilize the LS (the two-dimensional NaCl analogue) lattice at the experimentally determined surface coverage. In this paper we extend our study to determine the conditions necessary to form stable LS_2, LS_4 and LS_6 lattices, which have yet to be observed. Using a simple design rule that involves matching the distances between either large-large particles and large-small particles or large-small particles and small-small particles to correspond to the respective potential minima leads to predictions for size ratios that will form each desired lattice. Choosing constant values for the other parameters that govern the problem we predict stable LS_2, LS_4 and LS_6 lattices at relatively low surface coverages. Additional simulations show that the LS, LS_2 and LS_6 lattices are indeed stable structures at their predicted surface coverage, whereas the LS_4 lattice is a metastable structure at the predicted surface coverage. This study may be used as a guide for experimentalists in their search for these novel structures.

3.2 INTRODUCTION

The production of extremely small structures, beneath the limits of modern-day lithographic techniques, is an area of intense interest these days. Self-Assembly or "bottom up" methods of manufacture are being explored as an alternative means for forming nanoscopic structures as opposed to "top down" direct patterning methodologies. Ordered patterns of nanoparticles could be used directly, for example, as high density magnetic media,[23, 24] if the particle were ferromagnetic, or indirectly as templating agents.[25] Other potential applications for these ordered arrays include photonic devices[26] and meta-materials.[27]

Experiments performed by Kiely et al.[3, 4] showed that thiol-stabilized gold particles with distinct bimodal size distributions spontaneously order into two-dimensional superlattices. It was thought that hard-sphere interactions control the order-disorder transition, but it was found that hard-sphere entropic ordering does not occur in these systems.[1] We showed that the LS lattice was stable at the experimentally observed surface coverage if interparticle interactions in the form of van der Waals, osmotic, and steric forces were included.[28]

In this paper we extend our simulations in search of stable, two-dimensional LS_2, LS_4 and LS_6 lattices. We are able to estimate the size ratio and surface coverages that will lead to each desired stable lattice by matching two of the three distances corresponding to the pair-wise potential minimum (i.e., small-small particles, large-small particles, and large-large particles) to the geometry of each lattice structure. Next we run melting simulations for each lattice to fine tune the size ratio and surface coverage to determine under what conditions the structures are stable. These simulations will be useful to experimentalists in searching for these new structures.

The remainder of the paper is divided into four sections. First, we briefly review the details of the melting simulation. Then we discuss the method of predicting stable lattice structures. The results of the simulation are then compared with our predictions. Additionally, we include results of another simulation which determines if these structures are indeed stable or just long-lived metastable states. Finally, we conclude with a discussion of the results.

3.3 SIMULATION

The main simulation employed in this study is the melting simulation. These melting simulations are performed by replicating a perfect L_mS_n lattice and allowing the particles to diffuse according to the Metropolis Algorithm adjusting the step size to obtain 50% acceptance of moves.[11] The magnitude and direction of each move are selected from two uniform distributions. Moves that lead to overlap of the particles' hard cores or which are deemed energetically unacceptable by the Metropolis algorithm are rejected. Melting simulations were performed for the LS, LS_2, LS_4, and LS_6 lattices comprised of large and small colloidal particles with appropriate size ratios. For the purposes of this paper the size ratio is defined as $\sigma = R_S / R_L$, where R_S and R_L are the hard sphere radii of the small and large particles, respectively. The particles are allowed to diffuse for 500 000 cycles and the results are visually examined. A lattice is regarded as having melted if the particles stray well beyond their mean lattice positions. In practice it is very obvious to tell whether or not a structure has melted. If the structure did melt, the interparticle spacing is decreased or conversely the coverage is increased and the process is repeated. Typically, melting occurs in the first few thousand diffusion cycles, but near the melting coverage it takes considerably more diffusion cycles and is sometimes difficult to tell if melting will ever occur. We considered lattices that remained stable after 500 000 diffusion cycles as stable structures.

Due to the extremely large number of energetic calculations required for all the simulations, the process was sped-up with the creation of a look-up table. In addition, the overlap and energetic calculations were implemented using a grid of 16 cells to accelerate the computation. By dividing the simulation box into cells, only those cells in the vicinity of the particle of interest need to be investigated for energetic calculations and particle overlap. Melting simulation times were highly dependent on the surface coverage, i.e., low surface coverages melted after only a few minutes of simulation time or less than 1000 diffusion attempts, while others remained stable after 24 hours of simulation time or diffusion attempts on the order of 10^6.

The Interparticle Potentials

The interparticle potentials included in the simulations were van der Waals attraction along with osmotic and steric repulsions of the form proposed by Vincent et al. For simplicity, all potentials have been non-dimensionalized by thermal energy, kT, where k is the Boltzmann constant and T is the temperature of the system.

The van der Waals potential for two spheres of unequal radii r_i and r_j at a dimensionless center-to-center distance d is given by[12]

$$V_A(d) = -\alpha\left[\frac{2}{\left(s^2-4\right)} + \frac{2}{s^2} + \log\left(\frac{s^2-4}{s^2}\right)\right], \quad (1)$$

where $s^2 = 2d / (r_i + r_j)$ and the dimensionless parameter $\alpha = A_{12321} / (6kT)$. A_{12321} is the overall Hamaker constant between the cores of the particles, the stabilizing layers, and the solvent. A value of α = 3 corresponding to T = 298 K was used for all the simulations.

The osmotic and steric potential used in the simulations proposed by Vincent *et al.*[13] are given by

$$V_{osm}(d) = \beta(\varphi(d))^2 a\left(\delta - \frac{(d-2a)}{2}\right)^2 \qquad \delta < d - 2a < 2\delta, \quad (2)$$

$$V_{osm}(d) = \beta(\varphi(d))^2 a\delta^2\left(\frac{(d-2a)}{2\delta} - \frac{1}{4} - log\left(\frac{(d-2a)}{\delta}\right)\right) \qquad 0 < d - 2a < \delta, \quad (3)$$

$$V_{elas}(d) = \gamma\varphi(d)a\delta^2\left\{\frac{(d-2a)}{\delta}log\left[\frac{(d-2a)}{\delta}\left(\frac{3-\frac{(d-2a)}{\delta}}{2}\right)^2\right] - log\left(\frac{3-\frac{(d-2a)}{\delta}}{2}\right) + 3\left(1-\frac{(d-2a)}{\delta}\right)\right\}$$

$$0 < d - 2a < \delta, \quad (4)$$

where the two dimensionless parameters are given by $\beta = 4\pi R_s^3 / (\upsilon_1\sigma^3)$ and $\gamma = 2\pi R_s^3\rho / (M_w\sigma^3)$. The parameter υ_1 is the molecular volume of the solvent, $\phi(d)$ is the effective volume fraction of polymer in the adjacent layer, χ is the Flory-Huggins solvency parameter for the polymer, M_w is the molecular weight of the stabilizing moiety, and ρ is its density. Here R_s is the dimensional radius of the small particle, a is the dimensionless radius of the particle (if the interaction was between a large and a small particle the average of the two was used), and δ is the dimensionless thickness of the adsorbed polymer layer. The values used in the simulation are as follows: $\upsilon_1 = 1.77\times10^{-28}$

m^3, $\chi = 0.3$, $M_w = 3.35\times10^{-22}$ g/molecule, $\rho = 0.866$ kg/L, $R_s = 1.5$ nm (in one instance $R_s = 2.5$ nm), and $\delta = \sigma$. The volume fraction of ligand $\varphi(d)$ is given by

$$\varphi(d) = \frac{N_{ligand} A_{ligand} \sigma^2}{R_s^2 d^2}, \tag{5}$$

where N_{ligand} is the number of ligand molecules attached to the particle and A_{ligand} is the cross-sectional area of the ligand molecule. Values of these parameters used in the simulation are: $N_{ligand} = 398$ (small particle), $N_{ligand} = 398 / \sigma^2$ (large particle), and $A_{ligand} = 1.45\times10^{-19}$ m^2. The value of N_{ligand} for the small particle was obtained by determining how many decanethiol molecules could occupy the particle surface in an hcp formation. For interactions between large and small particles an average of the ligand volume fraction was used.

A hard-sphere cutoff limit was chosen as the interparticle spacing corresponding to the maximum of the interparticle potential (typically above 75 *kT*) and any sampling closer than this limit resulted in rejection. This not only served to exclude inaccessible phase space, but also slightly accelerated the simulation.

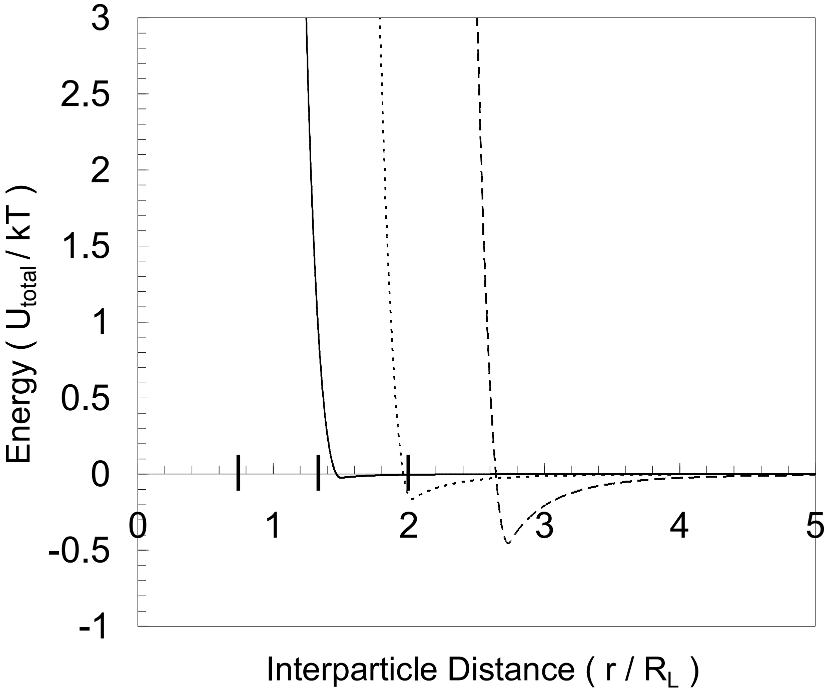

Figure 3.1: The interparticle potential for $\sigma = 0.375$ between two large particles (dashed-line), a large and a small particle (dotted-line), and two small particles (solid-line) using $\alpha = 6.04$, $\beta = 4\ 540$, $\gamma = 1.04\text{x}10^{-3}$, $\delta = 0.375$. Large bars on the x-axis indicate the hard sphere contact distance for the small-small, large-small, and the large-large respectively.

Figure 3.1 illustrates the interparticle potential for $\sigma = 0.375$. It should be noted that although this size ratio is not specifically used in the paper, it illustrates all of the following size ratios qualitatively. It should also be noted that our model for the interparticle potential is in good agreement with the recent findings of Saunders and Korgel,[8] both qualitatively and quantitatively.

There are three distinct potential curves corresponding to the interactions between two large particles, two small particles, and a large and a small particle. The large-large potential has the deepest well, a direct result of increased van der Waals attraction due to larger particle cores. Likewise, the small-small potential has a much shallower well because it has less polarizable material. As mentioned before, three dimensionless groups dominate this problem. The first α is a ratio of the energy due to the van der Waals interaction and the thermal energy in the system. The second dimensionless group β relates the osmotic energy with the thermal energy of the system. And the third dimensionless number γ relates the elastic energy with the thermal energy of the system. By tuning the values of these parameters we are able to tune the amount of thermal energy in the system.

A number of assumptions were employed in our work. First, since our initial studies were motivated by the experimental observations by Kiely *et. al.*[3, 4] we modeled our particles as being capped with decanethiol ligand and interacting through a toluene solvent. All parametric values used in the simulations are based on these realistic conditions. Second, we held the dimensional radius of the small particle fixed at 1.5 nm (unless otherwise specified) since this is near the smallest practical size of manufacturing nanoparticles. Additionally, the sizes of the periodic cells used in the melting simulations were sufficiently large to ensure that no effects were produced from a small sample size; doubling the size of the periodic cell produced the same stable structures. Finally, we assume a specific geometric arrangement for the particles as seen in Figure 3.2d of the next section, where d_{LL} bisects d_{SS} leading to eqns. (6-7). It is for this reason that we did not investigate the LS_3 or LS_5 lattices, which do not have such symmetric lattices.

3.4 PREDICTIONS

In our study of the self-assembly of bidisperse particles,[28] we noticed that the stability of the LS lattice was due, in large part, to the fact that nearest neighbor large-large particles sat in their potential minima as did the nearest neighbor large-small particles. In this case the distance between two small particles was so great that the interparticle potentials were negligible when compared with the other potentials. Later we noticed that in most cases only two of these potential minima can be satisfied at the expense of the remaining potential minimum. Figure 3.2 shows a central large particle surrounded by symmetrically located small particles corresponding to the LS, LS_2, LS_4, and LS_6 lattices.

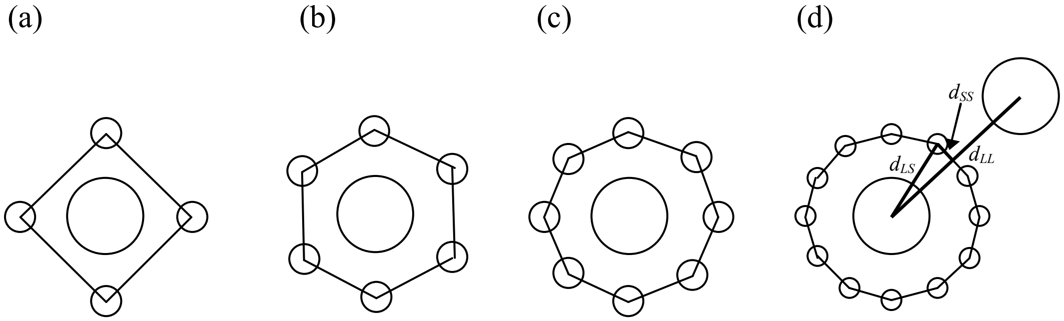

Figure 3.2: Locations of small particles surrounding a large particle for the (a) LS, (b) LS_2, (c) LS_4 and (d) LS_6 lattices. For the LS_6 lattice the location of the nearest large-large neighbor is shown along with the distances between large-large particles (d_{LL}), large-small particles (d_{LS}), and small-small particles (d_{SS}).

Each of these lattice structures has its own distinct ratios of distances between small-small particles, large-small particles, and large-large particles. Geometrically, this leads us to the relations:

$$\frac{d_{SS}}{d_{LS}} = 2\sin\left(\frac{\pi}{n_S}\right), \tag{6}$$

and

$$\frac{d_{LL}}{d_{LS}} = 2\cos\left(\frac{\pi}{n_S}\right), \tag{7}$$

where n_S is the number of small particles surrounding a large particle and d_{SS}, d_{LS}, and d_{LL} are the center-to-center distances between small-small particles, large-small particles, and large-large particles, respectively. Each is shown schematically in Figure 3.2d.

As mentioned earlier, the particles are modeled as interacting via van der Waals attraction and osmotic and steric repulsions, the combination of which gives an interaction potential, like that shown in Figure 3.1, with a distinct potential minimum for each of the pairs of nearest neighbor large-large particles, large-small particles, and small-small particles. Three dimensionless parameters govern the interactions. The first, α, is a ratio of the van der Waals interaction energy to the thermal energy of the system. The second, β, relates the strength of the osmotic repulsion between two particles. Finally, γ, is a measure of the strength of the steric repulsion between two particles. Since these dimensionless parameters are functions of σ and the other values set by the conditions of the experiment, the distance that corresponds to the location of each of the potential minima is strongly determined by the size ratio of the particles. The heart of the method of prediction lies in matching the geometric distances of either eqns. (6) or (7) (as stated before, typically only one of the two ratios can be satisfied at one time) with the actual potential minima as calculated from eqns. (1-4). This leads to a prediction of the size ratio and surface coverage for each desired bidisperse lattice. In this paper the surface coverage is defined as the total area of the particles' hard spheres divided by the simulation cell area.

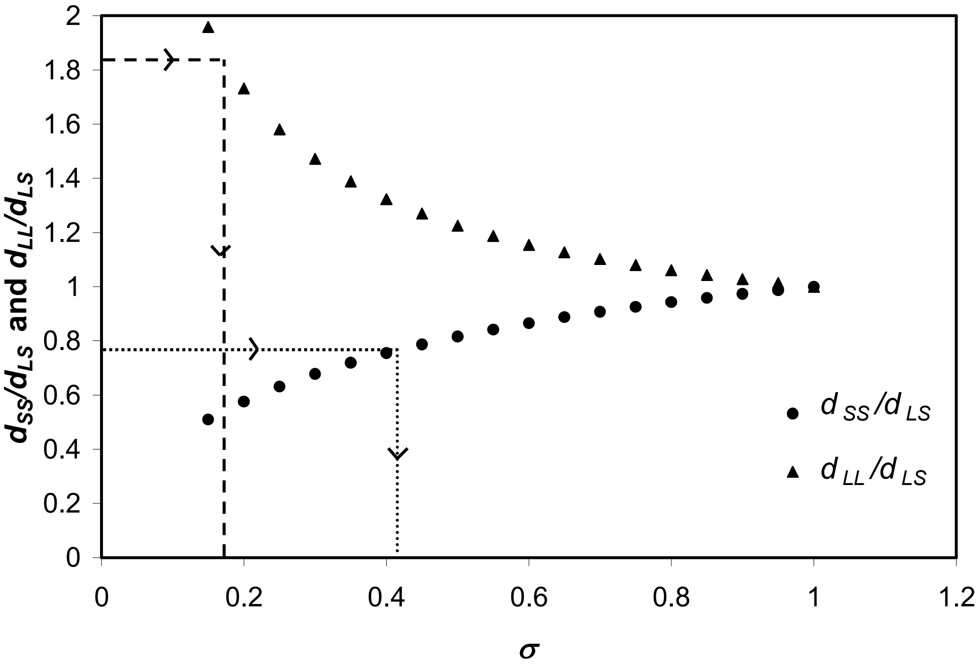

Figure 3.3: The distance corresponding to the potential minimum between small-small particles relative to the distance corresponding to the potential minimum between small-large particles (circles) and the distance corresponding to the potential minimum between large-large particles relative to the distance corresponding to the potential minimum between small-large particles (triangles) as a function of the size ratio (σ). The straight lines represent predictions of the size ratio for the LS_4 lattice when the aim is in minimizing the potentials between the nearest neighbor large-small and small-small particles (dotted line) and large-small and large-large particles (dashed line). Here $\alpha = 3$, $\beta = 240/\sigma^3$, $\gamma = 5.50 \text{x} 10^{-5}/\sigma^3$, $\delta = \sigma$.

Figure 3.3 shows the ratios of the distances corresponding to the potential minima between small-small and large-small particles, $d_{SS}^{min}/d_{LS}^{min}$, and the relative potential minima between large-small and large-large particles, $d_{LS}^{min}/d_{LL}^{min}$, as a function of the size ratio as calculated from the potentials. For each value of the size ratio, the potentials [eqns (1-4)] were calculated, the distances corresponding to the potential minima were determined for the large-large particles, the large-small particles, and the small-small particles and their ratios graphed. With this figure and eqns. (6) or (7) we are then able to predict the size ratio and surface coverage, which are reasonable starting points to search for stable lattices. The dotted and dashed lines of Figure 3.3 show the prediction for the size ratios of the LS_4 lattice. If the aim is to minimize the potentials between the nearest neighbor small-small and large-small particles, eqn. (6) gives $d_{SS}/d_{LS} = 0.77$. Following the dotted line off the $d_{SS}^{min}/d_{LS}^{min}$ curve leads to $\sigma = 0.416$. In the same manner, if the aim is to minimize the potential between nearest neighbor large-large and large-small particles, eqn. (7) gives $d_{LL}/d_{LS} = 1.85$. Following the dashed line off the $d_{LL}^{min}/d_{LS}^{min}$ curve leads to $\sigma = 0.172$. Table 3.1 gives a summary of all of the predictions for both cases of the satisfied ratios.

The size ratios σ^a and σ^b are those determined using Figure 3.3 and either satisfying the interparticle spacing for the large-large and large-small particles or for the large-small and small-small particles, respectively. The choice of σ^a or σ^b can be made based on the relative number of nearest neighbor large-large, large-small and small-small interactions per unit cell. For the LS and LS_2 lattices, σ^a provides a reasonable starting point for the search since the number of small-small interactions are relatively small compared to the others. For the LS_4 and LS_6 lattices, where there are relatively large numbers of nearest neighbor small-small interactions, σ^b proves to be a better starting point.

n	σ^a	σ^b	σ^{actual}	$\theta^{predicted}$	θ^{actual}
1	**0.333**	N/A	0.333	0.491	0.491
2	**0.200**	1.000	0.200	0.682	0.682
4	0.172	**0.416**	0.471	0.332	0.451
6	0.155	**0.154**	0.154	0.780	0.780

Table 3.1: Predicted values of the size ratio for an LS_n lattice minimizing the potential minimum between (a) large-large and large-small particles and (b) large-small and small-small particles. Values that were used as the starting points for the simulations are in boldface and were used in determining the predicted surface coverage ($\theta^{predicted}$). The final computed values from the simulations for the surface coverage (θ^{actual}) and size ratio (σ^{actual}) are also shown. $\alpha = 3$, $\beta = 240/\sigma^3$, $\gamma = 5.50\text{x}10^{-5}/\sigma^3$, $\delta = \sigma$.

In the first case, the LS lattice, the objective is to place the nearest neighbor large-large and large-small particles in their potential minima giving a starting point of $\sigma = 0.333$. For the LS_2 lattice, once again, the interest is in minimizing the potentials between nearest neighbor large-large and large-small particles, which leads to a predicted value of $\sigma = 0.20$. In each of the above cases it is obvious that the $d_{LL}^{min}/d_{LS}^{min}$ ratio is what should be used to predict the size ratios as satisfying the other ratio leads to unrealistic predictions, however it is not the case for the LS_4 or LS_6 lattices. In the case of the LS_6 lattice, it is unimportant exactly which ratio we satisfy because they both give an approximate starting point of $\sigma = 0.154$. For the LS_4 lattice there are two possible starting points, however $\sigma = 0.416$ was the only point that eventually led to a stable system at relatively low coverage.

3.5 RESULTS

The predictions of the preceding section were very helpful in identifying the values of θ and σ for the various lattice structures. For the LS, LS_2 and LS_6 lattices the predictions resulted in stable lattice structures without the need for adjustment. However, slight adjustments were necessary for the LS_4 lattice.

In this case, the dimensional radius of the small particle was increased to 2.5 nm and a new set of predictions were made with the method outlined above. This led to a prediction for the LS_4 lattice of $\sigma = 0.471$ and $\theta = 0.451$, which then resulted in a stable lattice. These predicted values appeared to be the most stable size ratios and are shown below. Figure 3.4 shows the melting simulations of all four of the lattice structures presented in this paper. Figure 3.4(a1-a2) shows the stability of the melting simulation for the LS lattice ($\sigma = 0.333$) using the predicted surface coverage of $\theta = 0.491$.

In our previous study of self-assembly[9] we were not able to computationally form a stable LS_2 lattice for the size ratio of 0.577. However, through our method of prediction, we were able to identify a different size ratio (0.20) that leads to a stable system. Figure 3.4(b1-b2) shows the stability of this LS_2 lattice ($\sigma = 0.20$). Figure 3.4(c1-c2) shows the stability of an LS_4 lattice ($\sigma = 0.471$) at a low surface coverage of 0.451. This is substantially lower than the other surface coverages for stable ordered lattices. Figure 3.4(d1-d2) shows the stability an LS_6 lattice ($\sigma = 0.154$) at the surface coverage of 0.780.

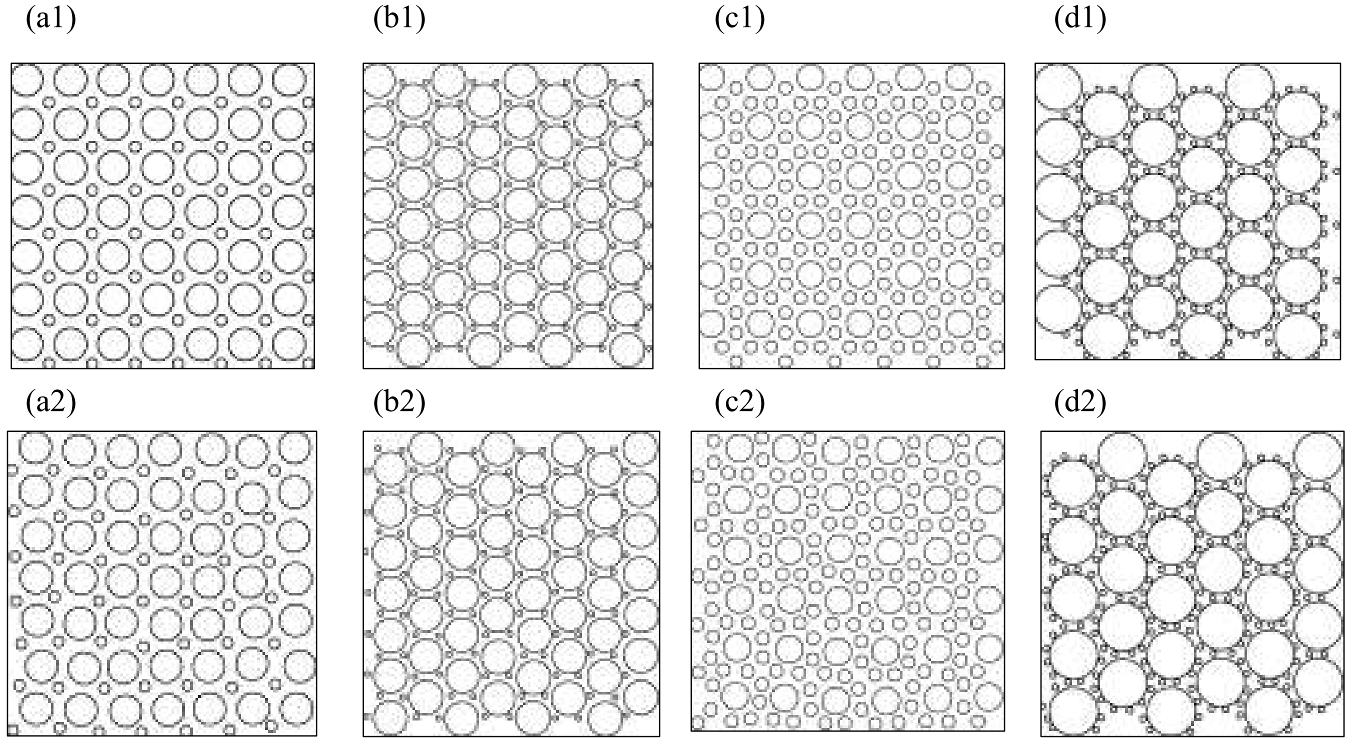

Figure 3.4: Stability of all 4 lattice structures. Stability of an LS lattice with $\sigma = 0.333$ and $\theta = 0.491$ after (a1) zero and (a2) 500 000 diffusion cycles. $\alpha = 3$, $\beta = 6\ 500$, $\gamma = 1.49\text{x}10^{-3}$, $\delta = 0.333$, $R_s = 1.5$ nm. Stability of an LS_2 lattice with $\sigma = 0.20$ and $\theta = 0.682$ after (b1) zero and (b2) 500 000 diffusion cycles. $\alpha = 3$, $\beta = 30\ 000$, $\gamma = 6.88\text{x}10^{-3}$, $\delta = 0.20$, $R_s = 1.5$ nm. Stability of an LS_4 lattice with $\sigma = 0.471$ and $\theta = 0.451$ after (c1) zero and (c2) 500 000 diffusion cycles. $\alpha = 3$, $\beta = 10\ 600$, $\gamma = 2.44\text{x}10^{-3}$, $\delta = 0.471$, $R_s = 2.5$ nm. Stability of an LS_6 lattice with $\sigma = 0.154$ and $\theta = 0.780$ after (d1) zero and (d2) 500 000 diffusion cycles. $\alpha = 3$, $\beta = 65\ 700$, $\gamma = 1.51\text{x}10^{-2}$, $\delta = 0.154$, $R_s = 1.5$ nm.

Several factors are attributable to the stability of these systems. The first is the size ratio. Figure 3.5 shows the result when the stable system of Figure 3.4b1 is changed from $\sigma = 0.20$ to $\sigma = 0.16$. After 104 000 diffusion cycles, the flight of small particles from their mean lattice positions is observed to disrupt the lattice.

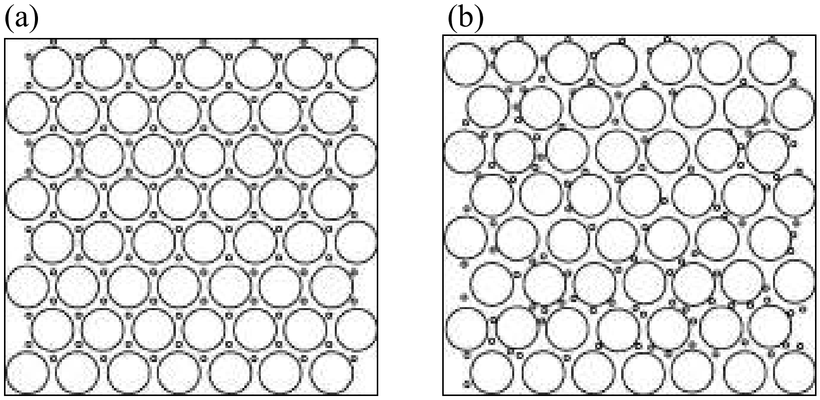

Figure 3.5: Instability of an LS_2 lattice with $\sigma = 0.16$ and $\theta = 0.682$ after (a) zero and (b) 104 000 diffusion cycles. $\alpha = 3$, $\beta = 58\ 600$, $\gamma = 1.34\text{x}10^{-2}$, $\delta = 0.16$, $R_s = 1.5$ nm.

A second factor that is responsible for the stability of a system is the dimensionless parameter β. Figure 3.6 shows what happens when the stable structure of Figure 3.4c1 is changed in such a way that the dimensional radius of the small particles are reduced from 2.5 nm to 1.5 nm (maintaining $\sigma = 0.471$ and $\theta = 0.451$). After 27 000 diffusion cycles the system is in disarray.

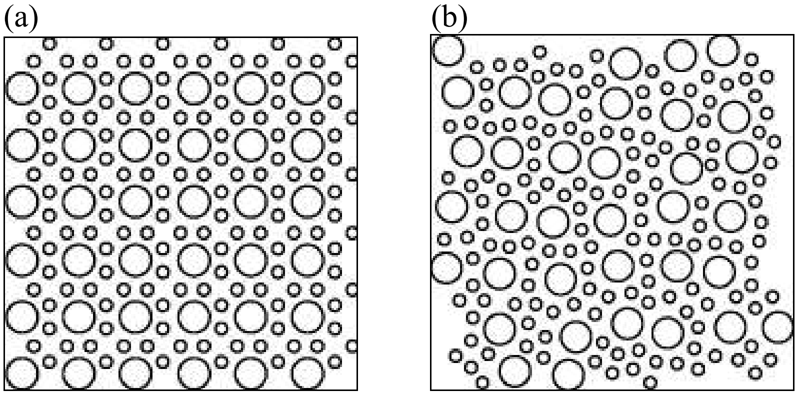

Figure 3.6: Instability of an LS$_4$ lattice with $\sigma = 0.471$ and $\theta = 0.451$ after (a) zero and (b) 27 000 diffusion cycles. The dimensional radius of the small particles has been reduced to 1.5 nm from the 2.5 nm small particles of Figure 3.4c1. $\alpha = 3$, $\beta = 2\,300$, $\gamma = 5.26\text{x}10^{-4}$, $\delta = 0.471$, $R_s = 1.5$ nm.

Returning to Table 3.1, it is seen that the initial predictions gave perfect estimates for the surface coverage in the case of the LS, LS$_2$, and LS$_6$ lattices which were used as the starting surface coverages for each of our simulations. The size ratio of the LS$_4$ lattice, on the other hand, did not lead to a stable lattice. However, when the dimensional radius of the small particle was increased to 2.5 nm a stable lattice is formed.

The question then arises as to whether or not these systems are truly stable states or if they are simply structures trapped in metastable states. To answer this question a periodic cell was created in which half of the cell consists of disordered phase while the other half consists of the ordered phase. All conditions remain the same for each individual lattice as in Figure 3.4, i.e. the same σ, θ, α, β, γ, and δ. Based upon the direction that the interface moves it is possible to tell whether the ordered phase is truly stable or rather just a metastable phase.

As seen in Figure 3.7, the interface of the LS lattice remains stable throughout the duration of the simulation concluding that it is indeed a stable structure.

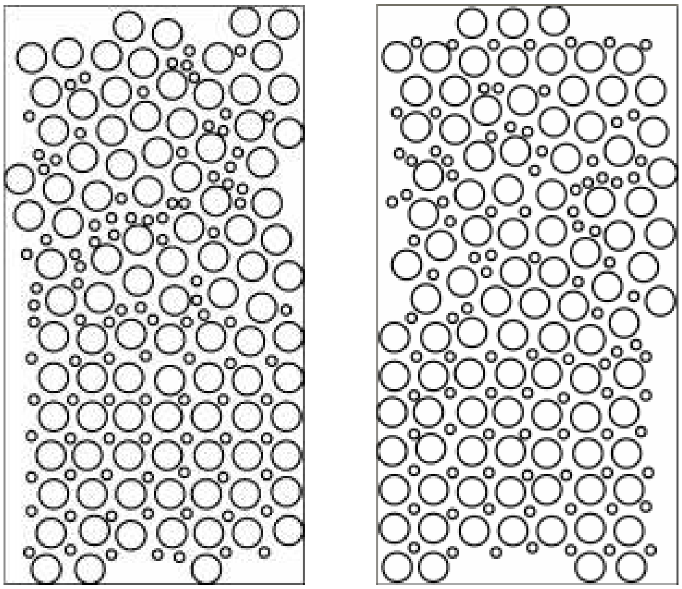

Figure 3.7: Stability of the interface between an LS lattice and disordered phase with $\sigma = 0.333$ and $\theta = 0.491$ after (a) zero and (b) 8 000 000 diffusion cycles. $\alpha = 3$, $\beta = 6\ 500$, $\gamma = 1.49\text{x}10^{-3}$, $\delta = 0.333$, $R_s = 1.5$ nm.

The LS_2 and LS_6 lattices encountered troubles when trying to obtain initial structures half ordered and half disordered phase for reasons not worthy of elaborating. However, when each of these cases were slowly compressed from a highly disordered low surface coverage ($\theta \sim 0.3$) to θ^{actual} – compression meaning a reduction in the periodic boundary size and a unilateral compression of all particle positions between diffusion steps – each resulted in the formation the respective lattice structure which persisted at that surface coverage. Therefore both of these lattices were determined to be stable structures.

As seen in Figure 3.8, the interface of the LS_4 lattice recedes until the entire system is disordered concluding that this lattice is a metastable state at $\theta = 0.451$.

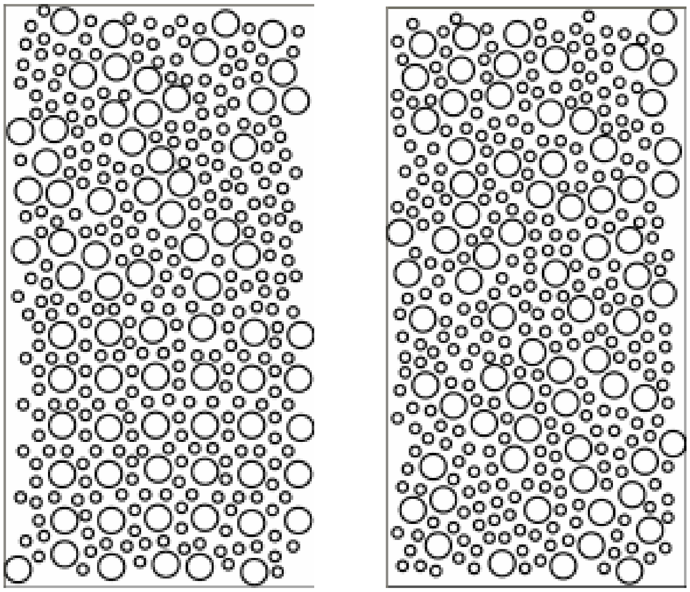

Figure 3.8: Instability of the interface between an LS_4 lattice and disordered phase with $\sigma = 0.471$ and $\theta = 0.451$ after (a) zero and (b) 1 000 000 diffusion cycles. $\alpha = 3$, $\beta = 10\,600$, $\gamma = 2.44\text{x}10^{-3}$, $\delta = 0.471$, $R_s = 2.5$ nm.

When the surface coverage was increased to $\theta = 0.50$, however, the interface of the LS_4 lattice remains stationary much like that of the LS lattice in Figure 3.7. Therefore, by increasing the surface coverage from $\theta = 0.45$ to $\theta = 0.50$ the LS_4 lattice changed from being merely a metastable structure to being a stable structure.

3.6 DISCUSSION

In each of the cases shown above the method of prediction gave values for the size ratios and surface coverages which resulted in stable lattices. The parameters estimated to form the LS, LS_2 and LS_6 lattices required no adjustment. However, for the case of the LS_4 lattice, the dimensional radius of the small particle had to be increased to 2.5 nm and new predictions made in order for the lattice to be stable.

As shown in the results section the values of σ and β play a large role in the stability of each lattice. Although not presented here, we have noted that in some cases that there is, not surprisingly, an envelope around the parameter values listed here that form ordered, bidispersed monolayers. A thermodynamic description of this envelope is unknown at this time, however, a few general guidelines may be of use to experimentalists when searching for these structures. Essentially three parameters were tweaked in the initial phases of this project: σ, α, and β. All others either had little effect on the stability (e.g. γ was usually overshadowed by β) or were an integral part of the model (e.g. changing the length of δ was a very involved process). To begin with, σ should be tweaked by a few hundredths around the initial value just to make sure the system is not just outside the stability range. Second, α can be varied by changing the particles' core material and/or the dispersing solvent (effectively changing the Hamaker constant). By increasing α the van der Waals force and the resultant potential well depth should increase leading to more stable configurations. Care should be exercised though as a potential well that is too deep leads to glassy clustering of particles. The last parameter, β, corresponds to the repulsive strength of the interaction and can be affected by changing the dimensional radius of the small particle. Few simulations were performed where this parameter was changed thus a good feel for how this parameter affects things was not obtained. However, as shown above, increasing the dimensional radius of the small particle did lead to stability in the LS_4 lattice.

The LS_3 and LS_5 lattices were not included since their lattice-units are not fully symmetric as is the case with all other lattices in our study. Since this quality contradicts our assumption that d_{LL} bisects d_{SS}, our prediction method is not applicable. This is not to say however, that stable lattice structures are not possible.

In all we have presented a method for predicting stable systems of bidisperse arrays of particles. An experimentalist, given any set interaction potential with a distinct minimum, would be able to use this method to predict a size ratio and surface coverage that would favor the formation of each lattice. From the interaction potential one would determine the large-large, large-small, and small-small distances corresponding to their respective potential minimum and, using our method outlined above, predict a size ratio and surface coverage favored to form the corresponding lattice structure. As an example we chose to look at decanethiol coated nanoparticles suspended in toluene. If an experimentalist wanted to observe structures in these systems they would need to match our dimensionless parameters governing the system, i.e. α, β, γ, and δ. As was mentioned before, we do not include an exact thermodynamic description of the system although we did present a few general guidelines as to how the system will react to changes in the size ratio and β.

To conclude we would like to emphasize that all of the parameters used throughout this paper are realistic and modeled after the experimental conditions set-forth in the papers of Kiely *et. al.*[6,7]. For example, the van der Waals interaction parameter, $\alpha = 3$, takes into account that the interaction is between two spheres surrounded by a decanethiol shell separated by a medium of toluene and conditions are room temperature. Likewise, the β and γ parameters involve values such as the density of toluene, $\rho = 0.866$

kg/L, and the molecular volume of the solvent toluene, $\upsilon_1 = 1.77\times10^{-28}$ m^3. Using these realistic values, for example, it is predicted that a LS$_6$ lattice consisting of 3.0 nm and 9.7 nm diameter particles with 1.5 nm thick ligand shells shows stability at a surface coverage of 0.781. It is hoped that this work will provide guidance and impetus to experimentalists to synthesize ordered nanoparticulate films.

Chapter 4. Observation of Long Range Orientational Order in Monolayers of Polydisperse Colloids

4.1 SUMMARY

Polydisperse amorphous-silicon colloidal particles ranging from approximately 10 to 140 nm in diameter were evaporated onto carbon substrates. The particles formed close-packed monolayers in which each particle had six-fold nearest neighbor coordination characteristic of a hexagonal lattice, yet completely lacked positional order. Orientational correlation functions were calculated for the particles and found to be constant throughout the aggregate, indicating the occurrence of long-range orientational order. Computer simulations revealed that the structural organization in this system resulted from capillary immersion forces that lead to a size separation as the particles deposit from the evaporating solvent onto the substrate.

4.2 INTRODUCTION

Colloids are technologically important materials with many industrial uses. Recent efforts have focused on the self-assembly of nanoscale colloids into "metamaterials" with unique properties.[29-31] For example, various superlattices with nanoscale compositional and spatial order have been made by simply evaporating the solvent from nanocrystal dispersions.[31] Non-spherical particles, such as rods and disks, also form close-packed structures, with orientational (as well as spatial) order.[32, 33] However, nanocrystal self-assembly depends on a complicated interplay of interparticle forces, packing constraints, and dynamics that are not yet well understood. As synthesis and theoretical and computational methods continue to advance, fundamental understanding of nanocrystal self-assembly also continues to rapidly develop.[1, 31, 34-37] However, one general perception of self-assembly is that polydispersity in size (and shape) destroys order.[38] In contrast to this perception, we demonstrate here experimentally and computationally that a highly polydisperse collection of colloidal particles can self-assemble into monolayers with long range orientational order, even in the complete absence of positional order. This unique structural organization results from both the size-dependent interparticle attractions and the dynamics of the monolayer formation process.

Long range orientational order without translational order is well-known in collections of nonspherical particles; for example, nematically ordered rods exhibit orientational order without positional order.[39] The hexatic phase is known for monolayers of monodisperse spherical particles,[40-42] which lacks long-range translational order but has relatively long range orientational order. We recently showed that certain kinetically-limited conditions can give hexatic order in monolayers of monodisperse hard spheres.[10] Here we show that an analogous structure exists for a collection of polydisperse spheres, which has long-range orientational order in the absence of positional order. The key to this kind of structural order is the polydisperse particle size distribution, which enables a gradual decrease in particle diameter from the center of the aggregate to its boundary. Computer simulations confirm that the size segregation results from lateral capillary forces in this system, which occur during the late stages of the drying process. As the solvent layer thickness decreases, the attractions between the large particles become sufficient to induce condensation while smaller particles have weak enough attractions to remain fluidized. Further evaporation induces attractive lateral capillary forces between particles with slightly smaller diameter, forcing them to collect at the aggregate edge, and so on, until all of the particles have collected at the edges of the aggregate and solvent has completely evaporated from the substrate.

4.3 EXPERIMENTAL DETAILS

Particle Formation.

Polydisperse amorphous silicon (*a*-Si) colloids were synthesized by thermal decomposition of trisilane in supercritical hexane (T_c=235°C; P_c=30 bar) at 500°C and 276 bar.[43] Trisilane and anhydrous hexane were obtained from Voltaix, Inc. (North Branch, NJ) and Aldrich Chemical Co. (St. Louis, MO), respectively and were stored in a nitrogen glove box. Trisilane (1 mM) in hexane was heated was thermally decomposed in the presence of supercritical hexane in a high pressure titanium batch reactor (inner volume 10 mL). The reaction temperature and pressure (500°C; 276 bar) were reached by insertion of the titanium reactor into a brass block heated via cartridge heaters. Extreme caution must be taken to avoid over-pressurizing the reactor, which is a closed system and could explore if the pressure tolerances are accidentally exceeded! Upon completing the reaction, the titanium reactor was cooled in an ice bath and the product was then extracted with chloroform. The particles disperse readily in organic solvents and were purified by centrifuging the reaction mixture at 9000 rpm for 10 minutes to precipitate impurities. The particles remain suspended in the supernatant and were collected for analysis. X-ray diffraction of the colloidal product confirmed that the particles are composed of amorphous Si.[43] The particles exhibit broad size distributions that do not exhibit Gaussian, log normal or Weibull distributions (Fig. 4.2), ranging from ~15 nm to ~150 nm in diameter (average diameter of 50 nm), and disperse in organic solvents.

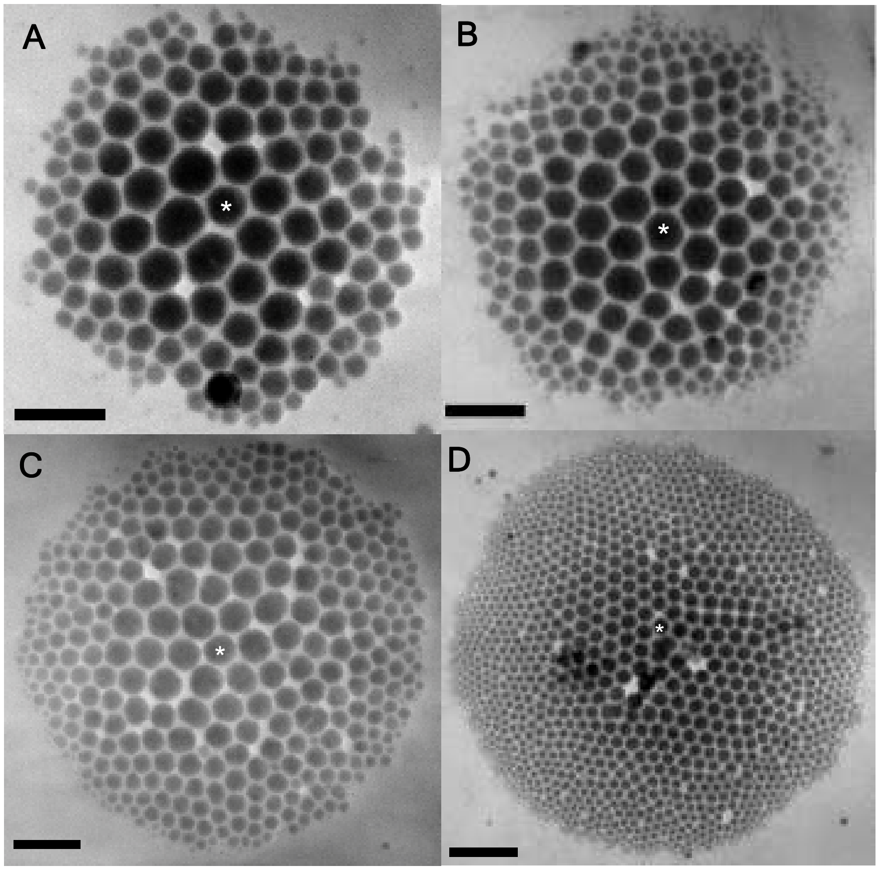

Figure 4.1: Transmission electron microscopy (TEM) images of amorphous silicon particles evaporated from chloroform. The aggregates in A, B, C and D have 135, 202, 330 and 1247 particles, respectively, with average particle diameters of 60, 52, 51 and 53 nm, respectively. The asterisk labels the reference particle used to calculate $g_6(r)$. Scale bars for A, B and C are 200 nm and the scale bar for D is 400 nm. The images were obtained on a JEOL 2010F field-emission electron microscope operating at 200 kV. Samples were prepared by drop casting chloroform dispersed particles on carbon-coated 200 mesh Cu grids (Electron Microscope Sciences).

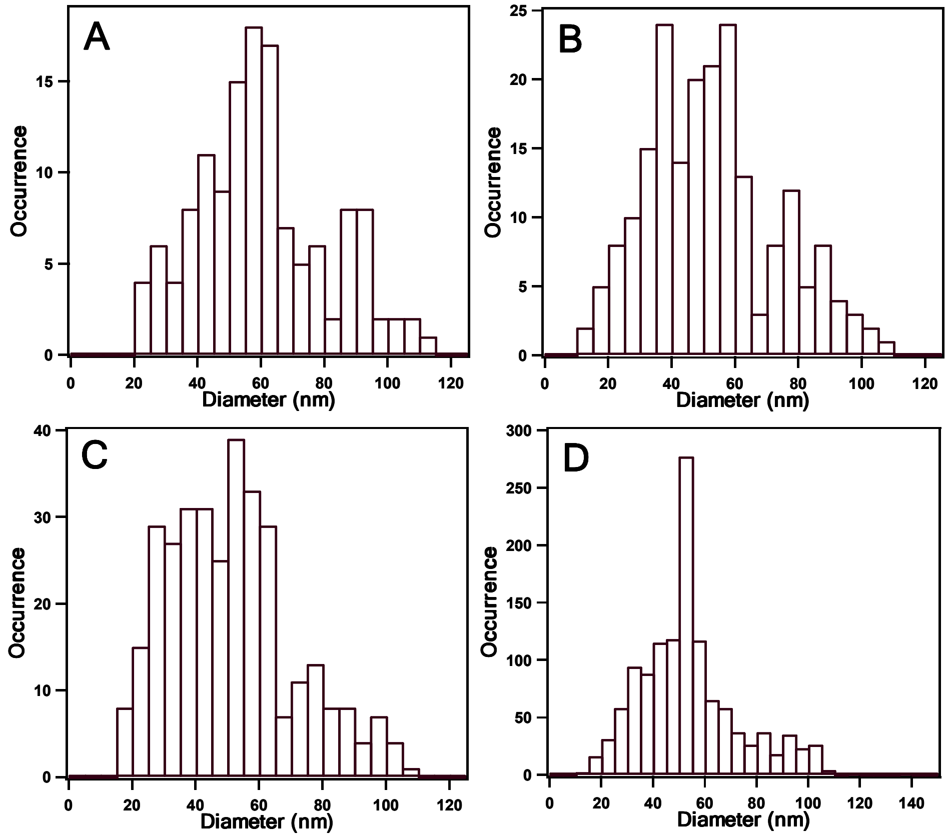

Figure 4.2: Histograms of the particle diameter from the TEM images in Figures 4.1A-D. The size distributions do not follow Gaussian, log normal or Weibull distributions. The size distribution obtained by sizing over 2000 particles in a particle synthesis is similar to the size distribution obtained from the large aggregate in Figure 4.2D.

Characterization

The a-Si particles were imaged by high-resolution transmission electron microscopy (HRTEM) on a JEOL 2010F field-emission electron microscope operating at 200 kV. HRTEM samples were prepared by drop casting chloroform dispersed particles on carbon-coated 200 mesh Cu grids (Electron Microscope Sciences).

4.4 RESULTS AND DISCUSSION

Figure 4.1 shows four transmission electron microscopy (TEM) images of aggregates of polydisperse colloidal particles composed of amorphous Si that were dispersed in chloroform and then evaporated onto a carbon-coated TEM grid. The particles form monolayers shaped like circular "droplets" that are relatively extended, up to ~2 μm in diameter with ~1250 particles. Size segregation occurs within the aggregates.

The size distributions of the particles imaged in Figure 4.1 are very broad and there is no positional order in the aggregates, yet there is long range orientational order. Each particle has six hexagonally close-packed nearest neighbors—*regardless of its location in the aggregate*—which is apparent in the orientational distribution functions $g_6(r)$,[44] calculated for the aggregates in Figure 4.1 plotted in Figure 4.3.

$g_6(r)$ provides the probability that each particle has exactly 6 close-packed nearest neighbors with perfect hexagonal symmetry and can be defined as $g_6(r) = \left|\psi_6^*(0)\psi_6(r)\right|$, where $\psi_6(r)$ is the complex order parameter for each particle j: $\psi_6(r) = \frac{1}{z}\sum_k \exp(6i\theta_{jk})$.[41, 45] θ_{jk} is the orientation angle of the line connecting the center of particle j and its z nearest neighbors, k, with respect to a fixed reference axis. If a particle has perfect hexagonal packing with 6 nearest neighbors ($z = 6$), each with an orientation angle of $\theta_{jk}/k = \pi/3$ (60°) with respect to the fixed reference axis, then ψ_6 has a maximum value of 1.

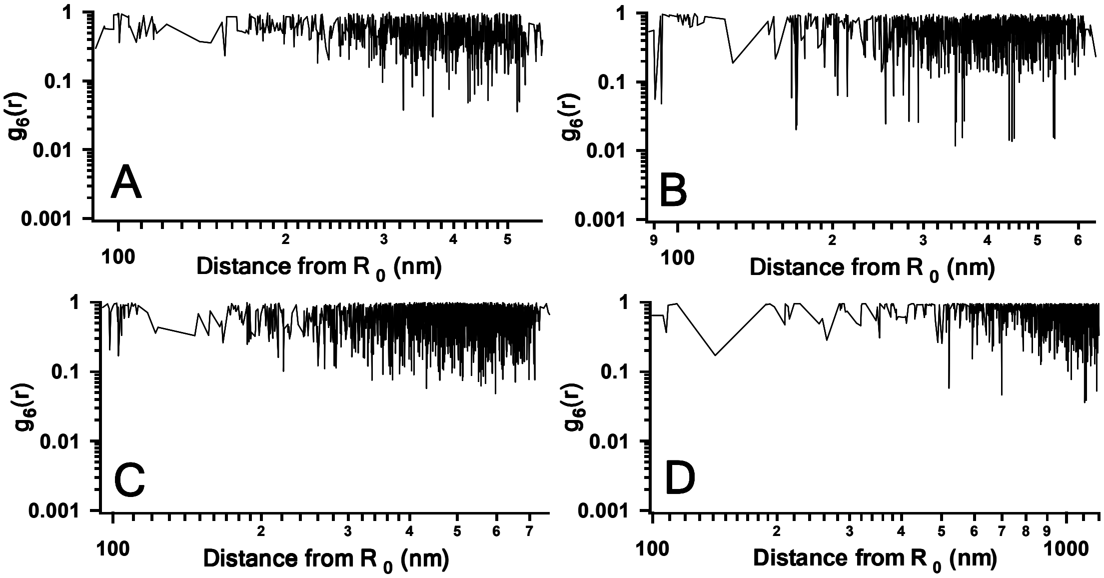

Figure 4.3: Orientational correlation functions, $g_6(r)$, calculated from the TEM images in Figures 4.1A-D using the particle labelled with an asterisk (*) as the reference particle. For the aggregates in Figures 4.1A, 4.1B and 4.1C, $g_6(r)$ was also calculated using the central particle's 6 nearest neighbors as reference particles and averaged.

Figure 4.3 shows $g_6(r)$ plotted against the center to center distance from the reference particle(s) to every other particle in the aggregate. The reference particles are labelled with asterisks in Figure 4.1. For the structures in Figures 4.1A, 4.1B and 4.1C, $g_6(r)$ was averaged using 7 different reference particles. For these discrete systems, only centrally located particles can be used as reference particles since $g_6(r)$ is radially symmetric and the use of an off-center particle or one near the edge as a reference particle skews the orientational correlation function. Figure 4.3 shows that

$g_6(r)$~constant, which indicates long range orientational order extending to the edge of the aggregate. Although there are examples of size segregation in evaporated colloid films,[22, 46, 47] there is no quantitative analysis that has rigorously revealed such a system with long-range order.

We hypothesized that capillary immersion forces were responsible for the observed structures and tested this with a Monte Carlo simulation incorporating a solvent film height-dependent capillary immersion attraction and a stabilizing repulsion between particles. Lateral capillary forces[48] arise between particles partially immersed in a thin liquid film, which occur as solvent evaporation nears completion and the particles become pinned to the substrate and distort the air-liquid interface. Lateral, or immersion, capillary forces can be significant for particles as small as 10 nm, which differs from capillary flotation forces,[49, 50] which are insignificant for particles smaller than 10 μm.[51] Simulations were performed by placing particles randomly in a two-dimensional 5625 D^2 square simulation cell (D is the diameter of the largest particle) with periodic boundary conditions. The number of particles, their size and size distribution, were specified to match the experimental conditions. Particles were allowed to move according to the Metropolis algorithm[11] and initially the solvent height l_0, was set equal to the largest particle diameter. To simulate solvent evaporation, l_0 was lowered by 0.0375% after 1000 lateral particle diffusion cycles. This slow evaporation ensures that particles have time to structurally "equilibrate" before again lowering the solvent height.

The interparticle potential depends on the solvent height and was calculated at each evaporation step as the sum of an attractive capillary immersion energy and a short-range repulsion: $U_{tot} = U_{cap} + U_{rep}$. The repulsive energy U_{rep}, was estimated to have a short-range exponential decay:

$$U_{rep}^{ij} = U_0 \exp\left[-\left(L - \left(R_i + R_j\right)\right)/\lambda\right], \tag{1}$$

where L is the center-to-center distance between particles i and j with radii R_i and R_j. λ is the distance over which the short-range repulsion acts and was set to 0.02. The capillary immersion energy between particles i and j, U_{cap}^{ij}, was calculated using a superposition approximation:[48]

$$U_{cap}^{ij} = -2\pi\sigma Q_i Q_j K_0\left(qL\right) \tag{2}$$

K_0 is a Bessel function, Q_k are the "capillary charges" of particles k, σ is the solvent surface tension and q^{-1} is the "capillary length." For thin films, $q^2 = -\Pi'/\sigma$, where Π' is the derivative of the disjoining pressure, $\Pi = A_H/(6\pi l_o^3)$, with respect to the solvent height, l_0. A_H is the Hamaker constant of the solvent. For chloroform, $\sigma = 0.0271$ N/m and $A_H = 2 \times 10^{-20}$ J.[52] Q_k relates to the contact line radius r_k, and the meniscus slope angle ψ_k, at the contact line with each particle: $Q_k \equiv r_k \sin(\psi_k)$.[48] r_k and ψ_k were determined by simultaneously solving two nonlinear equations:

$$r_k(h_k) = [(l_0 + h_k)(2R_k - l_0 - h_k)]^{1/2}, \tag{3}$$

$$h_k = -r_k(h_k)\sin(\psi_k)\ln\left[\gamma_e q r_k(h_k)/2\right], \tag{4}$$

given that $\psi_k = \arcsin(r_k/R_k) - \alpha_k$, where α_k is the contact angle and $\gamma_e = 1.781072418\ldots$ is the Euler-Masceroni number. h_k is the elevation of the contact line at the sphere's surface. The particles were assumed to be perfectly wetting such that $\alpha_k = 0$. Each subsequent round of diffusion proceeds with updated potentials and to accelerate the computation, the surface was divided into 36 grid cells and only neighboring cells were considered when calculating potentials.

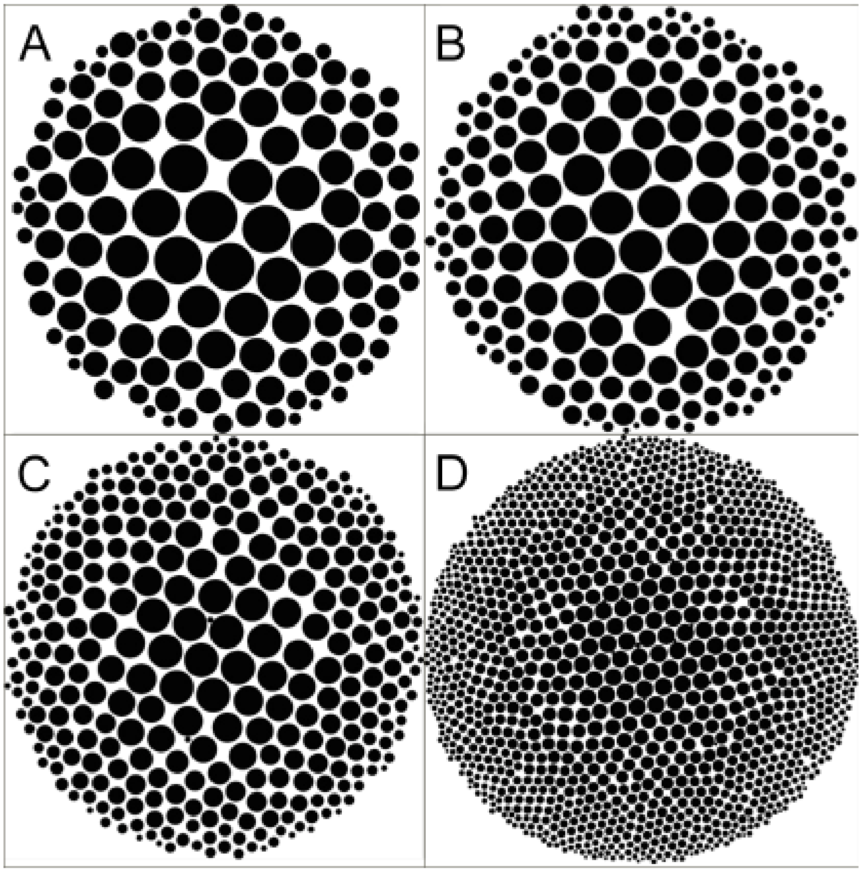

Figure 4.4: Simulation results. The size and numbers of particles in each simulation were made to match the respective histogram of Figure 4.2. Capillary immersion energy and simple stabilizing repulsion were the only energies included in the simulation. For the simulations, $\sigma = 0.0271$ N/m, $A_H = 2 \times 10^{-20}$ J, and $\alpha_k = 0$.

Figure 4.4 shows the simulated microstructures. They are strikingly similar to the experimentally observed structures. The size segregation occurs because solvent evaporation induces significant capillary attractions first between the largest particles in the distribution, which leads to their aggregation once these attractions exceed the thermal energy U_{KE}, of the system. At a given solvent film height, the ratio of lateral capillary attractions, U_{cap}^{ij}, between "big" (*B*), "medium" (*M*), and "small" (*S*) particles is proportional to their size:

$$\frac{U_{cap}^{BB}}{U_{cap}^{BM}} \approx \frac{R_B}{R_M} > 1 \ , \quad \frac{U_{cap}^{BM}}{U_{cap}^{MS}} \approx \frac{R_B}{R_S} > 1 \ \text{and}\ U_{cap}^{MS} < U_{cap}^{BM} < U_{cap}^{BB} \quad . \tag{6}$$

Initially, when $l_0 = 2R_B$, the lateral capillary attractions are weak and the kinetic energy of the system U_{KE}, is sufficient to keep the particles fluidized. As the solvent evaporates, U_{cap} increases until eventually $U_{cap}^{MS} < U_{cap}^{BM} < U_{KE} < U_{cap}^{BB}$, at which point the big particles aggregate. More evaporation eventually leads to $U_{cap}^{MS} < U_{KE} < U_{cap}^{BM} < U_{cap}^{BB}$ and the medium particles aggregate. Continued evaporation leads to the aggregation of small particles with the aggregate. Note that $U_{cap}^{BM} > U_{cap}^{MM}$, which implies that the medium particles aggregate with the large particles before homogeneous aggregation occurs between medium particles. Likewise, $U_{cap}^{MS} > U_{cap}^{SS}$, and smaller particles stick to the edge of the growing aggregate of big and medium particles as opposed to aggregating homogeneously with other small particles.

4.5 CONCLUSIONS

The size-segregated aggregation in Figure 4.1 results from the size-dependence of the lateral capillary forces that occurs during the evaporation process. Figure 4.5 provides a schematic of the formation of these structures. Interestingly, the polydisperse aggregate exhibits long-range orientational order, despite the complete absence of positional order. Others have also observed qualitatively similar size segregation for polydisperse colloids evaporated onto substrates, although the orientational correlation functions have not previously been reported.[22, 46, 47] Ohara, *et al.*[22] and Antonietti, *et al.*[46] attributed their observed size separation to size-dependent van der Waals (vdW) attractions; whereas, Yamaki, *et al.*[47] attributed size segregation to immersion capillary forces and ignored vdW attractions. In the case of our *a*-Si colloids, the lateral capillary forces almost certainly dominate over the vdW attractions. The vdW attractions between dispersed a-Si particles ($U_{vdw}=-A_HR/(12h)$, where h is the surface to surface separation of the particles, A_H is the interparticle Hamaker constant (~6.04×10^{-20} J), at a center-to-center separation of $3R$) is less than the lateral capillary attraction between particles when the solvent height falls to about ¾ of the diameter (the approximate solvent height that results in particle addition to the nucleus as seen in the simulations) until the particle size is reduced to ~2.4 nm in diameter. In the particle size range considered here, lateral capillary forces induce the observed size segregation.

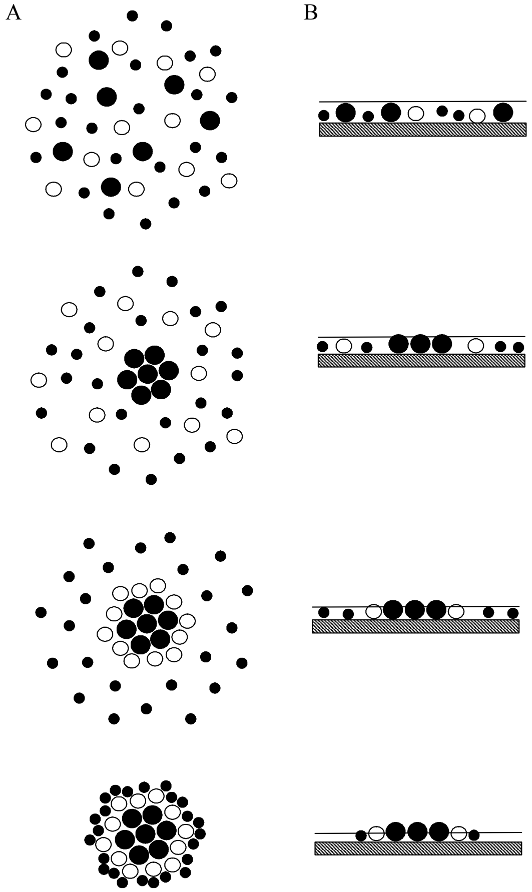

Figure 4.5: Schematic of particle assembly through lateral capillary forces. A. Top-down view of the self-organization. B. Side view of the self-organization. In the first row the particles are completely submerged and there are no lateral capillary forces acting on the particles. In the second row the fluid height is sufficiently low so that there are menisci on the largest particles. This creates a lateral capillary force, drawing the large particles together forming the nucleus of the forming structure. In the third row the fluid film has dropped below the tops of the medium-sized white particles and enacts a lateral capillary force drawing these particles to surround the newly formed nucleus. In the final row the fluid film has dropped below the tops of the smallest particles and the resulting capillary forces have drawn them to surround the outer rim of the polydisperse structure.

Chapter 5. A Computational Study of the Hydrodynamically-Assisted Organization of DNA-Functionalized Colloids in 2D

5.1 SUMMARY

We study computationally the self-organization of DNA-functionalized colloidal particles confined to two dimensions and subjected to a linear shear force. We show that hydrodynamic forces allow a more thorough sampling of phase space than thermal or Brownian forces alone. Two particle types are present in each of our dynamic simulations each signifying its own specific oligonucleotide sequence grafted to the particle surface: A-type and B-type. Particles are modeled as interacting via a type-specific DNA attraction where unlike-types have affinities for each other while like-types do not. The particles are small enough to feel Brownian motion while the shear adds motion to the particles. We find the formation of lines of A-type and B-type particles in simulations with an imposed shear. Simulations without imposed shear form a frustrated network with little or no linear order. An orientational distribution function, $g_2(r)$ quantifies the degree of linear order. A phase diagram is constructed, finding a linear dependence of the minimum DNA force necessary for line formation on the dimensionless shear rate. A force analysis performed on the structures shows that the lines orient perpendicular to the axis of the elongation component of the shear because it is this orientation that allows the DNA attraction to resist the shear.

5.2 INTRODUCTION

As the feature size of new devices continues to decrease so too does the feasibility of top -down methods of patterning them. In many cases bottom-up methods are replacing the existing methods of assembly, as having building blocks self-organize into the desired structure appears, in many cases, to be a much more advantageous route.

Self-assembled nanoparticulate films have a wide range of potential applications; high-density magnetic media, sensing arrays, meta-materials[27] and as seeds for 3D photonic crystals[53] to name a few. Thus, it is critical that we understand the fundamental dynamics of pattern formation on the nanoparticulate and colloidal scale so that we may have better control over the formation and final quality of these structures.

In our previous study[1] we used Monte Carlo simulations of bidisperse hard disks to study the experimental observation of highly-ordered 2D arrays of bidisperse, stabilized gold nanoparticles.[3, 4] Our finding, however, was that kinetic limitations prevented the formation of these structures with hard disks alone. Later, we showed that the addition of interparticle forces along with a simple compression leads to the formation of 2D LS lattices;[28] the main finding of the study being that the assembly of these lattices structures is a dynamic process. This scheme was later extended to predict size-ratios and surface coverages favoring the formation of novel bidisperse 2D lattice structures.[36]

In each of the above cases the thermal motion imparted on the particles is the primary means of exploring phase space. This means of sampling works well when the pairwise interparticle potential is on the order of *kT*, however, many instances dictate pairwise potentials far exceeding this value. In these circumstances, a large external forcing could potentially aid in sampling phase space where thermal energy falls short.

Specifically, we look to hydrodynamics as a new tool for the effective sampling of phase space in structures where the interparticle potentials far exceed *kT*.

The energy of the hydrogen bond between Guanine and Cytosine (G-C) in a double stranded DNA molecule is approximately 3 kT.[54] For short segments of DNA containing a number of base pairs (bp) the total binding energy can easily exceed 10s to 100s of kT. Recently, there has been much success with the DNA-assisted self-assembly of micron-sized[55-59] and even nanometer-sized particles.[60] The general approach involves the grafting of a number of short segments of a particular DNA sequence to the surface of a particle (creating a certain particle type) and grafting a second, different DNA sequence to the surface of another particle (creating a second particle type). Typically, a short strand of DNA complimentary to both grafted sequences, referred to as a linker, is added to the solution and enables the hybridization. Many variations of this technique exist including grafted sequences that are rigid or flexible, double or single stranded linkers, and even no linker at all (the grafted sequences are complimentary and link themselves). The major advantages of this DNA-assisted method of assembly include its incredible specificity for interparticle interactions, a great tunability of the interactions, and the reversibility of the process. A theoretical study was recently performed for a binary system of this type, finding the possibility of a number of surprising lattice structures.[61]

The conventional method used for controlling the hybridization of DNA-functionalized particles has focused on the manipulation of the solution temperature. An elevation of the solution temperature beyond the hybridization temperature of DNA leads to the dissociation of DNA strands, reversing the agglomeration of particles. When the solution temperature then returns below the hybridization temperature the DNA segments can rehybridize resulting in particle agglomeration.[55-60] This method of manipulating the solution temperature gives a great deal of control over the reversible hybridization of the

DNA-functionalized particles; however, it is not inherently obvious that the specific particles within the structure itself are achieving a highly organized state without the help of other, involved techniques such as the asymmetric functionalization of nanoparticles[21] and the DNA-directed synthesis of binary nanoparticle networks.[62]

In this paper we follow the role of hydrodynamic shear as a new method for sampling phase space for DNA-functionalized colloidal particles confined to the interface of two fluids. We show that hydrodynamic assistance offers a new tool to more thoroughly sample phase space than with thermal assistance alone.

5.3 SIMULATION

Problem Statement

We consider a system of Brownian particles confined to the interface of two fluids. Two types of particles are considered: A-type and B-type particles (denoted black and white in Figure 5.1). All particles experience a short ranged repulsion at close separations, modeled as the osmotic repulsion attributed to overlapping ligands. Unlike particle-types also experience an attractive force due to the hybridization of DNA sequences when the particles are within a specified distance of each other. The like particle-types do not experience this attractive force. In this way each particle-type models a different sequence of grafted DNA and captures the very specific interactions of the DNA-hybridization technique. The particles are small enough that thermal forces are significant and thus experience a random Brownian force. Additionally, linear shear in the plane of the particles adds motion to the particles.

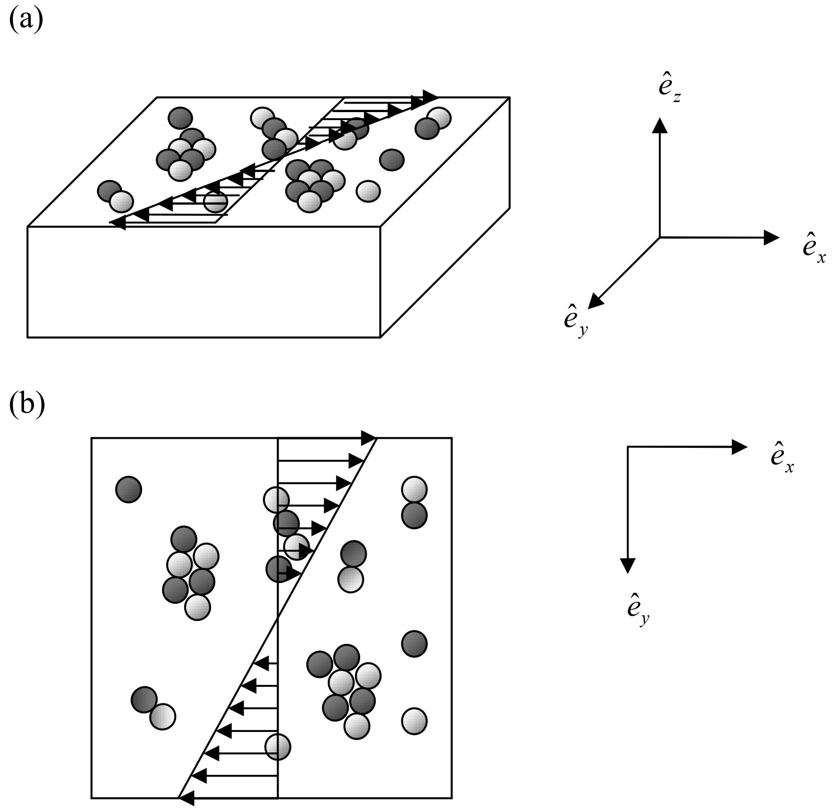

Figure 5.1: The problem setup for the dynamic simulation. A-type and B-type (dark and light) colloidal particles are situated at the interface of two fluids. All particles experience a short ranged repulsion at close separations, modeling the osmotic repulsion attributed to overlapping ligands. Unlike particle-types experience an attractive force due to the hybridization of DNA sequences when the particles are within a specified distance of each other. The like particle-types do not experience this attractive force. The particles are small enough that thermal forces are significant and thus experience a random Brownian force. Additionally, linear shear in the plane of the particles adds motion to the particles. (a) 3D view of the problem. The particles are confined to the xy-plane. (b) Top-down view of the problem.

The particles' movements are determined using the Langevin equation:

$$\underline{\dot{x}}_i = \underline{\underline{M}}_i \cdot \left(\underline{F}_i^P + \underline{F}_i^B \right) + \underline{U}_i^\infty , \tag{1}$$

where $\underline{\dot{x}}_i$ is the velocity of particle *i*, $\underline{\underline{M}}_i$ is the mobility tensor of particle *i*, $\underline{F}_i^P$ are the particle forces acting upon particle *i*, $\underline{F}_i^B$ is the Brownian force acting on particle *i*, and $\underline{U}_i^\infty$ is the external fluid velocity at the position of particle *i*.

The interparticle forces, $\underline{F}_i^P$, are comprised of an osmotic repulsion, $\underline{F}_i^{Osm}$, and an attractive DNA force, $\underline{F}_i^{DNA}$.

$$\underline{F}_i^P = \underline{F}_i^{Osm} + \underline{F}_i^{DNA} \tag{2}$$

The osmotic repulsion is modeled as an exponential decay:

$$\underline{F}_i^{Osm} = F_0 \exp\left(\frac{-\left(d_{ij} - 2a\right)}{\zeta} \right) \underline{e}_{ij} , \tag{3}$$

where F_0 is the maximum force, d_{ij} is the center to center distance between particle *i* and particle *j*, *a* is the particle radius and ζ is the repulsive decay length. The attractive DNA force is represented by

$$\begin{aligned} \underline{F}_i^{DNA} &= -F_{DNA} \underline{e}_{ij} && if \quad d_{ij} \le 2L_{DNA} \\ \underline{F}_i^{DNA} &= 0 && if \quad d_{ij} > 2L_{DNA} \end{aligned} \tag{4}$$

where F_{DNA} is the force of the DNA attraction and $2L_{DNA}$ is the length of the hybridized DNA segments. This representation of the attractive DNA force was chosen since it was shown that the potential energy of the DNA attraction scales linearly with the interparticle separation.[59]

The Brownian Forces are modeled with the ensemble averages

$$\left\langle \underline{F}^B(t) \right\rangle = 0 \qquad \left\langle \underline{F}^B(0) \underline{F}^B(t) \right\rangle = 2\underline{\underline{M}}^{-1} \delta(t) , \tag{5}$$

where $\delta(t)$ is the Dirac delta function.

The external fluid velocity is represented as a linear shear:

$$\underline{U}_i^{\infty} = \dot{\gamma}\underline{x}_i \cdot \underline{e}_y , \tag{6}$$

where $\dot{\gamma}$ is the shear rate and $\underline{x}_i$ is the position of particle *i*.

The equations are non-dimensionalized as follows:

$$\hat{\underline{F}}_i^P = \frac{a\underline{F}_i^P}{kT} = \frac{aF_0}{kT}\exp\left(\frac{-\left(\hat{d}_{ij}-2\right)}{\zeta / a}\right)\underline{e}_{ij} - \frac{aF_{DNA}}{kT}\underline{e}_{ij} \tag{7}$$

$$\hat{\underline{\underline{M}}} = 6\pi\mu a\underline{\underline{M}} , \tag{8}$$

$$\hat{\underline{x}}_i = a\underline{x}_i \tag{9}$$

$$\hat{t} = \frac{kT}{6\pi\mu a^3}t \tag{10}$$

$$\hat{\dot{\gamma}} = \frac{6\pi\mu a^3}{kT}\dot{\gamma} \tag{11}$$

where μ is the viscosity of the fluid, *a* is the particle radius. The dimensionless Langevin equation, then, is simply

$$\Delta\hat{\underline{x}} = \hat{\underline{\underline{M}}} \cdot \hat{\underline{F}} \cdot \Delta\hat{t} + \hat{\dot{\gamma}} \cdot \hat{\underline{y}} \cdot \Delta\hat{t} . \tag{12}$$

The key dimensionless parameters that describe the system are $aF_o/(kT)$ – the dimensionless repulsive force, $aF_{DNA}/(kT)$ – the dimensionless DNA force and $6\pi\mu a^3\gamma/(kT)$ – the dimensionless shear rate.

The explicit expression for the dimensionless mobility tensor is given by

$$\hat{M} = \underline{\underline{I}} ,$$

where $\underline{\underline{I}}$ is the 2-by-2 identity matrix. Here we assume a constant Stokes drag on the particles regardless of the concentration. At high concentration, the most important hydrodynamic force in shear is the lubrication interaction. The short-ranged repulsive force in equation (3) prevents particle overlaps much like a hydrodynamic lubrication interaction for particles near contact, and so this effect is included in the simulation.

The Numerical Algorithm

The Langevin equation is discretized using a midpoint algorithm, which calculates the new position of the particle in a two-part step.

$$\underline{x}_{i*} = \underline{x}_{it} + \frac{1}{2}\underline{\underline{D}}(\underline{x}_{it}) \cdot \left[\underline{F}_i^P(\underline{x}_{it}) + \underline{F}_i^B(\underline{x}_{it})\right]\Delta t \tag{13a}$$

$$\underline{x}_{i,t+\Delta t} = \underline{x}_{it} + \underline{\underline{D}}(\underline{x}_{i*}) \cdot \left[\underline{F}_i^P(\underline{x}_{i*}) + \underline{F}_i^B(\underline{x}_{i*})\right]\Delta t \tag{13b}$$

where $\underline{x}_{it}$, $\underline{x}_{i*}$ and $\underline{x}_{i,t+\Delta t}$ are the positions of particle i at the beginning, midpoint and end of the step. Re-evaluating the diffusivity and deterministic forces at the midpoint increases the accuracy of the solution and correctly accounts for the variation of diffusivity in space.[63]

The Simulation Details

A and B-type particles are added to the interface in a 1:1 ratio via the random sequential adsorption method. The motions of the particles on the surface are integrated forward in time between each adsorption attempt. Once the desired surface coverage is attained no more particles are adsorbed, however, the positions continue to evolve and are monitored for a period thereafter. Lees-Edwards boundary conditions are used[64] to ensure a continuous linear shear profile.

The parameters used in the simulation were chosen with the intent of modeling the experimental systems found in the literature.[60] The osmotic repulsion was simplified through its representation as an exponentially decaying repulsion (Equation 3) using the dimensionless parameters $aF_o/(kT) = 923$ and $\zeta/a = 0.13$ - a fit of the osmotic potential typical for a particle 13 nm in diameter.[13] These repulsive parameters will remain fixed for the remainder of the paper. Typical DNA hybridization energies are approximately 2.1 kT for each base pair (bp) involved.[54] In the literature, a linkage of approximately 20

- 30 bps is used with approximately 1 to 2 interconnects per particle[60] justifying our choice of DNA energies on the order of 10s of kT with dimensionless DNA lengths of $L = 0.5$. The energies can however, be lessened through variations in the solution temperature.[55] There are also notable examples of reduced hybridization energies such as the use of an RNA kissing complex,[65] so we include these lesser values in our studies as well.

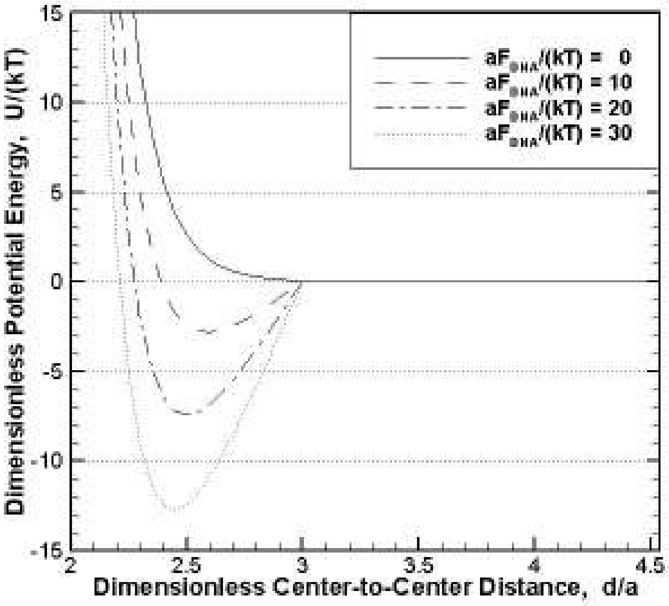

Figure 5.2: The pairwise potential between an A and a B-type particle for various values of the dimensionless DNA force. The repulsive force remains constant with parameters $aF_o/(kT) = 923$ and $\zeta/a = 0.13$. The solid-line ($aF_{DNA}/(kT) = 0$) is equivalent to the pairwise potential between two like-type particles and consists solely of the repulsive potential.

Figure 5.2 shows the pairwise potential energy between an A and a B-type particle. As the dimensionless DNA force increases so also does the potential well-depth. In the range of interest, the well-depth of the pairwise potential is multiple *kT*s making thermal sampling largely ineffective and forcing us to look towards hydrodynamic assistance.

To expedite the pairwise summation of the interparticle forces, the simulation cell is divided into smaller grid cells and only neighboring grid cells are included in the computation. In the following microstructures presented in the results section, each simulation cell contains anywhere from 120 to 360 particles.

The microstructures are displayed, however, with the simulation cell periodically replicated on three of the surrounding edges. The entire structure that will be viewed is now composed of four replicated simulation cells with bordering edges denoted by the lines within each of the figures. This not only aids the eye in the identification of linear order but also verifies the fidelity of the Lees-Edwards boundary conditions. Simulations were performed with upwards of 1000 particles and the same phenomena were observed, affirming that our choice of simulation cell size has little effect on each of the results. Typical simulations were run on an Intel Xeon 3.0 MHz processor and lasted anywhere from one to three days with the rate-limiting step being the adsorption of particles to the desired coverage. To ensure reasonable run times, the desired surface coverage was set at 95% of the predicted surface coverage for a crystalline lattice with minimum potential energy.

5.4 ANALYSIS

The orientational order of a system can be quantified using the orientational distribution function, $g_n(r)$, defined as

$$g_n(r) = \langle \psi_n^*(0)\psi_n(r) \rangle , \tag{14}$$

where ψ_n is the complex order parameter for each particle j. ψ_n is defined as

$$\psi_n = \frac{1}{z}\sum \exp(ni\theta_{jk}) , \tag{15}$$

where θ_{jk} is the orientation angle between the reference particle j and each neighboring particle k. The summation is over all z neighboring particles.

Typically, $g_6(r)$ is used to quantify the orientational order of a 2D monodisperse system since each disk should have exactly 6 neighboring disks in a perfect hexagonal crystal. In our case, however, the interest is on the development of linear arrays of A and B-type particles. For this we use a $g_2(r)$ parameter. More specifically, for each reference particle, the $g_2(r)$ only regards other like-type particles when performing the calculation (e.g. when calculating the ordering parameter of an A-type reference particle all B-type particles are deliberately overlooked). Figure 5.3 shows the microstructure and the corresponding $g_2(r)$ for a perfect linear array of A and B-type particles.

The $g_2(r)$ for a truly perfect lattice has infinitely tall peaks at each of the given locations. Our system, however, has undergone a few extremely short diffusion cycles, intentionally slightly spreading the peaks of the orientational function. The defining characteristic of linear order displayed by the $g_2(r)$ is the existence of a large initial peak followed by two closely-spaced, smaller peaks. It is these closely spaced second and third peaks that we use to quantify the degree of linear order in our systems. Figure 5.3c illustrates the corresponding locations of each of the individual peaks. The asterisk denotes the reference particle.

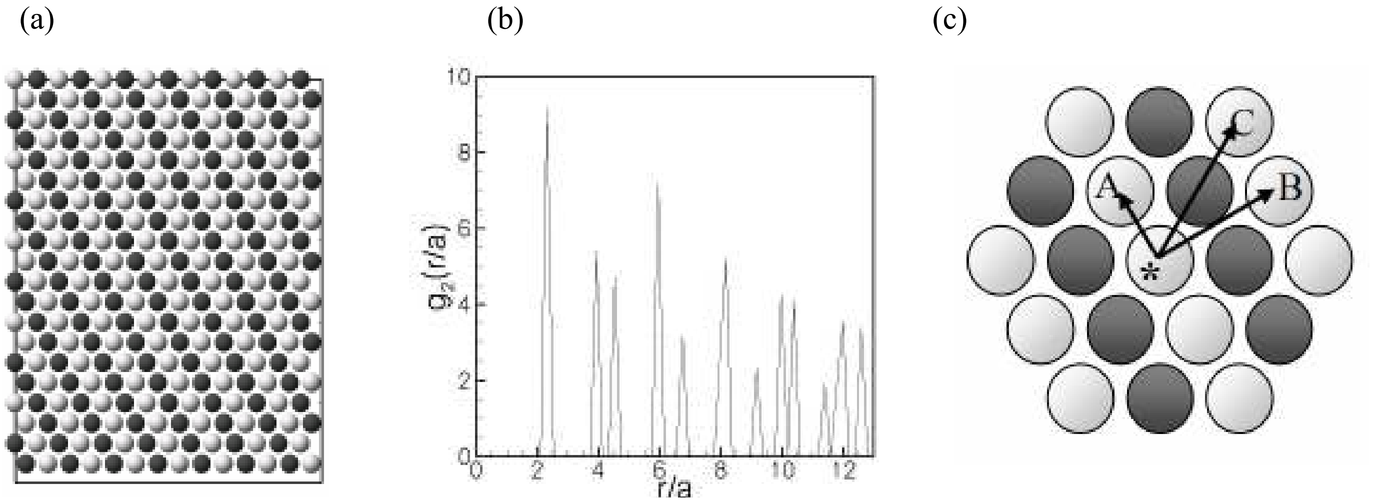

Figure 5.3: (a) The microstructure of a perfect 2D crystal displaying lines of A and B-type particles and (b) the corresponding $g_2(r)$. (c) Diagram of a perfect hexagonal lattice displaying lines of A and B-type particles. The reference particle is denoted by (*) in the figure. The distances from this reference particle to particles A, B, and C represent the first three peaks in the $g_2(r)$ data, each respectively.

The distance from this reference particle to particle A denotes the distance corresponding to the first and largest peak. It is understandable that this distance corresponds to the largest peak as it is this close proximity which should preserve the largest degree of order. The second peak is represented by the next closest distance on the figure; that of the reference particle to B. In the same way, the third peak corresponds to the remaining distance; the reference particle to C. Once again, it is these last two peaks which will be used in the determination of the linear order of a system.

Figure 5.4 contrasts three individual microstructures with varying degrees of linear order (Decreasing order from left to right). The three microstructures are all from the same simulation but each is taken at a different time throughout the run. The corresponding $g_2(r)$ data for each microstructure is shown below. The microstructures show a reduction in linear order (from left to right) as confirmed by the $g_2(r)$ data - shown as a reduction in the second and third peaks.

For the purposes of this paper we define a microstructure as lacking linear order if the second and third peaks do not surpass a set value of 0.5. Setting the cutoff at 0.5 is not arbitrary; we have noticed through the careful examination of various, different microstructures that this is the point where the microstructures form linear order. Later in the results section, simulations are run using specific values for the DNA force and the shear rate and the results analyzed to determine if the predetermined conditions give rise to the linear arrays; the overall aim being the construction of a phase diagram. In this case, the conditions of the system are said to give rise to linear arrays if just one of the microstructures' $g_2(r)$ data surpasses this threshold of 0.5. This is done because it is a highly improbable event that a condition corresponding to disorder will serendipitously form the linear arrays. Any indication of formation is considered the ability to form.

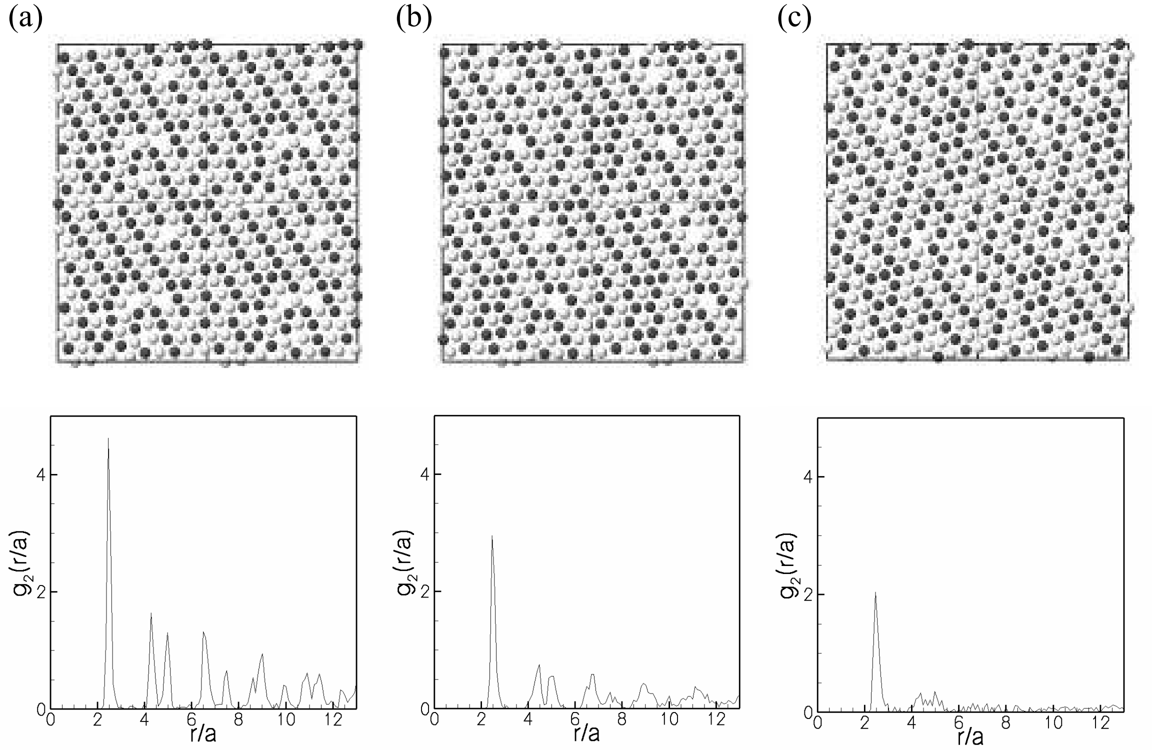

Figure 5.4: Three contrasting microstructures and their corresponding $g_2(r)$ data for (a) t = 119.871, (b) t = 117.309 (c) t = 114.372. The microstructures show a reduction in linear order (from left to right) as confirmed by the $g_2(r)$ data - shown as a reduction in the second and third peaks. $\theta = 0.56$, $aF_{DNA}/(kT) = 20$, $aF_o/(kT) = 923$, $\zeta/a = 0.13$ and $\gamma = 0.1$.

5.5 RESULTS

The first condition that is considered is one whose motion is limited to thermal sampling. No shear is imposed and the Brownian and interparticle forces are the only means of movement for the particles. Figure 5.5 shows a representative image of the resulting microstructure along with the corresponding $g_2(r)$. Notice that the microstructure contains many linked A and B-type particles however very little linear order is observed. The $g_2(r)$ data is more conclusive and shows the complete absence of the second and third peaks. When a simulation is run under these conditions a general trend emerges. As particles are adsorbed to the surface, Brownian motion carries particles within range of other particles where the interparticle forces take action. At close separations the DNA attraction causes unlike particles to stick to one another. As further particles are added, these new particles are carried by Brownian motion towards the existing structures, sticking and ultimately forming a large network of particles. Once stuck, particles in this frustrated network remain fixed, since the Brownian forces are not large enough to drive readjustment against the strong DNA attraction.

The result is a large network of linked particles with very limited ordering. Even a drastic reduction in the adsorption rate (Effectively increasing the amount of diffusion before adsorption) is futile. The particles are destined to form a frustrated network of A and B-type particles lacking a significant degree of order.

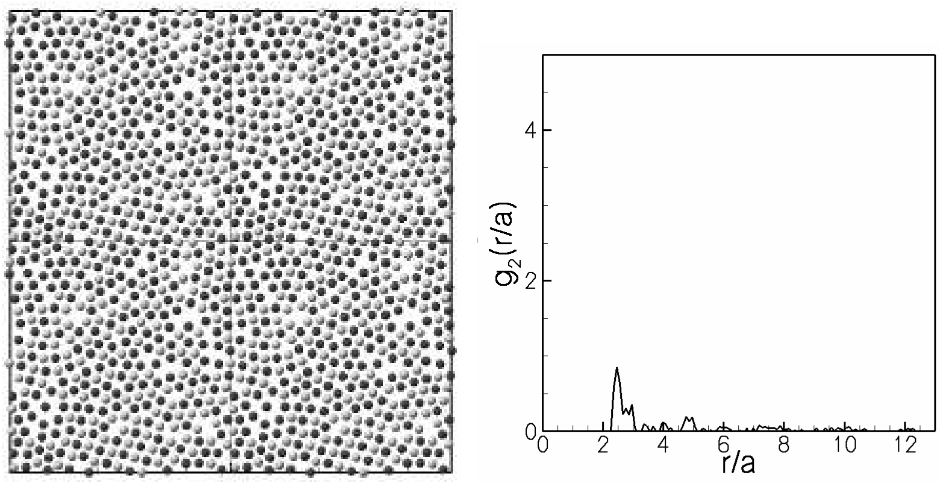

Figure 5.5: The resulting microstructure of maximum order for a simulation run without shear forces and the corresponding $g_2(r)$ data. $N = 363$, $aF_{DNA}/(kT) = 30$, $aF_o/(kT) = 923$, $\zeta/a = 0.13$ and $\gamma = 0$.

In the second simulation considered, all conditions of the previous one are preserved with exception to the addition of a linear shear. Particles are random sequentially adsorbed to the surface until the surface coverage of the previous simulation is attained and the system continues to be monitored throughout 10 shear-cycles. We define each shear-cycle as the time it takes for a trace particle at the top of the periodic box to travel through the periodic boundary edges and return to its initial starting location (Brownian forces neglected). By observing a given number of shear cycles we are guaranteed to observe the effect of even the slowest shear rates on the development of each microstructure. Figure 5.6 shows the resulting microstructure and corresponding $g_2(r)$ data when shear forces are applied.

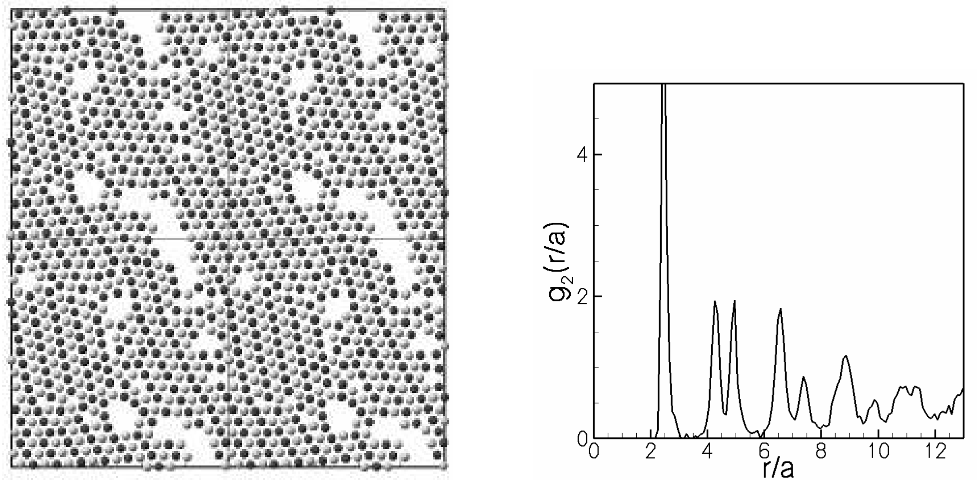

Figure 5.6: The resulting microstructure of maximum order for a simulation run with shear forces and the corresponding $g_2(r)$ data. $N = 363$, $aF_{DNA}/(kT) = 30$, $aF_o/(kT) = 923$, $\zeta/a = 0.13$, and $\gamma = 0.1$.

As before, the A and B-type particles become linked together. This time, however, there is a much higher degree of order seen in the microstructure and heavily affirmed by the $g_2(r)$ data. Multiple rafts are readily visible throughout the entire microstructure. It is the shear force that is driving the alignment of particles as it is the only differing element between the two simulations. Through the observation of many different microstructures under a variety of conditions we noticed that the lines tend to orient perpendicular to the axis of the elongation component of the shear. In the discussion section we provide an explanation as to why this is the most stable form. Additionally, a majority of the simulations forming linear arrays show the breakup and regeneration of order throughout the duration of each simulation run. Specifically, the $g_2(r)$ data shows an oscillation in the degree of linear order with a period of approximately 1 shear cycle.

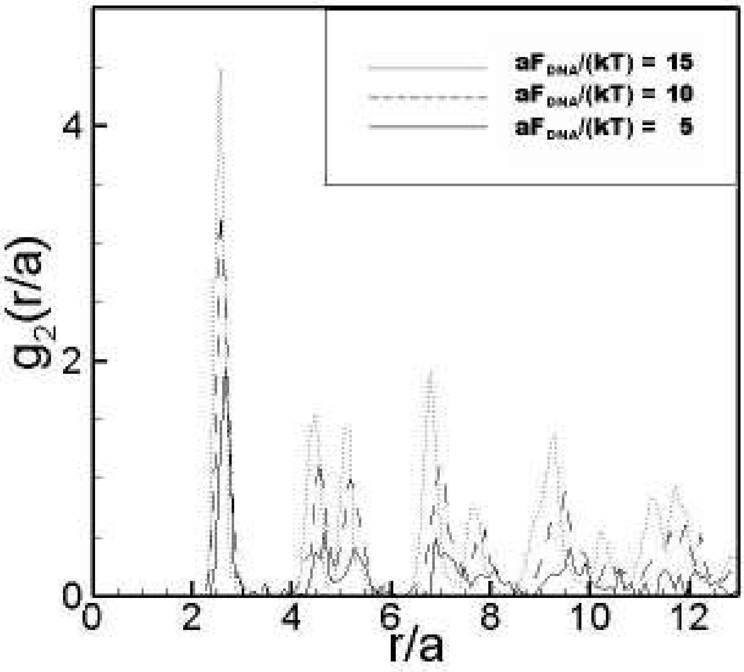

Figure 5.7: $g_2(r)$ results corresponding to the microstructures of maximum order for various values of the dimensionless DNA force. A reduction in the dimensionless DNA force to 5 results in the loss of linear order (as set by our guidelines). $aF_o/(kT) = 923$, $\zeta/a = 0.13$ and $\gamma = 0.1$.

The formation of linear arrays must be a result of - at the least - the interaction of the DNA attraction and the shear force. As the DNA force is reduced there must be a value at which the formation of linear arrays will cease; since a reduction in the DNA force to 0 makes particle-types indistinguishable. To probe the effect of the DNA force on the formation of linear arrays we fixed the shear rate and incrementally decreased the strength of the DNA attraction. The resulting $g_2(r)$ data corresponding to the microstructures of maximum order are shown in Figure 5.7. It is evident that a reduction in the dimensionless DNA force causes a reduction in the overall linear order of the microstructure. This is seen in the reduction of the second and third peaks of the $g_2(r)$. Specifically, for a dimensionless shear rate of $\gamma = 0.1$ we get the order/disorder transition occurring somewhere between $aF_{DNA}/(kT) = 10$ and $aF_{DNA}/(kT) = 5$.

A phase diagram was then constructed by varying the dimensionless shear rate as well as the dimensionless DNA force; observing whether or not linear order is present in each case. The resulting phase diagram is shown in Figure 5.8.

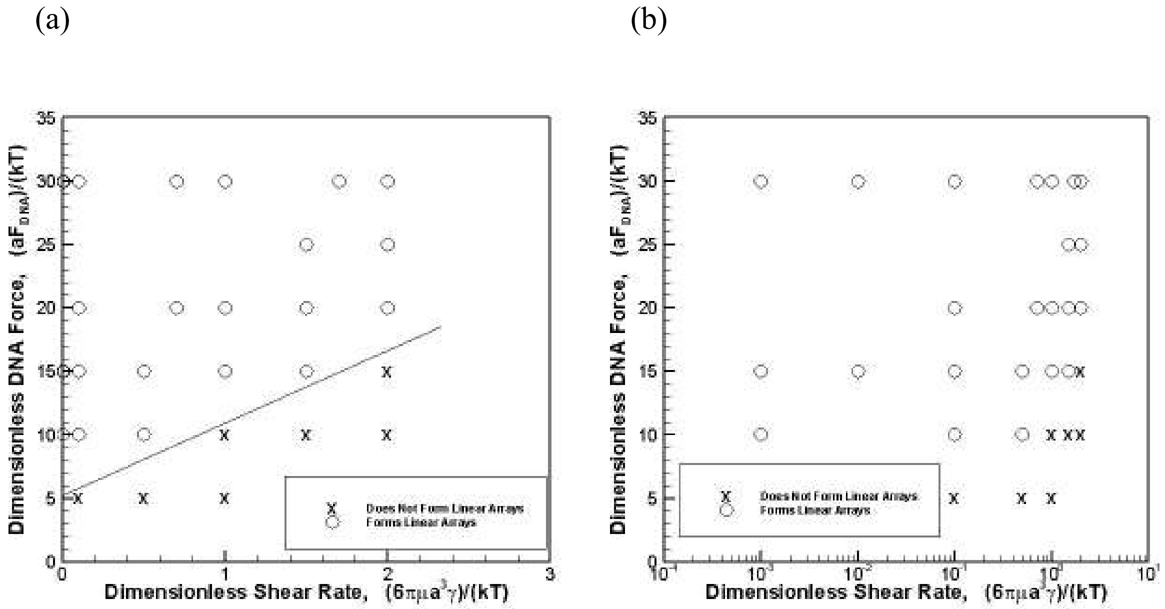

Figure 5.8: Phase Diagram displaying the formation of linear arrays as (a) a standard plot and (b) a logarithmic plot.. For each data point A and B-type particles were random sequential adsorbed in a 1:1 ratio until the desired surface coverage was reached and the particles were sheared for 10 shear-cycles. The $g_2(r)$ data was then analyzed and, depending on the heights of the second and third peaks, linear order was determined. $aF_o/(kT) = 923$ and $\zeta/a = 0.13$.

The figure shows the general trend offered earlier; that a reduction of the DNA attraction results in a reduction of linear order. The phase diagram also shows that an increase in the shear rate hinders the linear order of a system. The order/disorder transition results from an interplay of the DNA attraction and the shear force and is fit by a straight line (overlaid in Figure 5.8). The reasons for this and an explanation of some of the other observed phenomena are addressed in the following section.

Simulations were also performed for a system which was modeled after experiments involving micron-sized particles.[55] In these cases, the value of L_{DNA} is approximately an order of magnitude less, leading to a very sharp interparticle potential-well thus requiring a much shorter time step for accurate computation. Because of this limitation, we were unable to observe the standard of 10 shear cycles for accurate analysis; however we did see evidence of the same linear array formation phenomenon for $aF_{DNA}/(kT) = 500$, $aF_0/(kT) = 3000$ and $\zeta/a = 0.01$.

5.6 DISCUSSION

The observation that lines orient perpendicular to the axis of the elongation component of the shear is not an obvious result. To understand why the particles assume this orientation, a simple analysis is performed focusing on two layers of alternating A and B-type particles. The particles within each layer are fixed relative to that layer (each particle placed at the distance of the potential minimum) and the vertical distance between the two layers remains fixed as well. Only horizontal shifts of each layer relative to the other are allowed. Figure 5.9 is a diagram of the proposed setup.

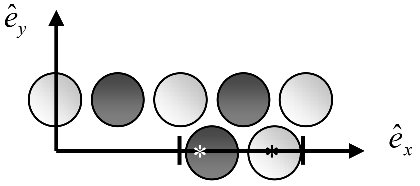

Figure 5.9: Two layers of alternating A and B-type particles. The particles within each layer are fixed relative to that layer and the vertical distance between the two layers is maintained. Only horizontal shifts of each layer relative to the other are allowed. The pairwise interactions between all of the particles in the top layer and these reference particles (denoted by *) are summed to arrive at the resultant force acting between the two layers. Specifically, the force that is calculated is the force exerted on the top row of particles by the two reference particles. The tick marks on the x-axis represent one cycle.

The particles marked by asterisks denote the reference particles. The pairwise interactions between all of the particles in the top layer and these reference particles are summed to arrive at the resultant force acting between the two layers. Specifically, the force that is calculated is the force exerted on the top row of particles by the two reference particles. When the entire top layer is displaced a value Δx from its starting position a new resultant force is calculated based upon the new relative locations of each of the particles. This can be done incrementally until a displacement of $2d$ (d being the center-to-center distance between particles in the same layer) is reached. At this point the particles have returned to the initial relative positions. In this way the force versus displacement curves are cyclical with a period of $2d$. The curves for various values of the dimensionless DNA force are shown in Figure 5.10. The letters A thru E on the curve represent various configurations for the two sheared layers and displayed to the right of the graph. The plot contains two sections in which the top layer has a positive force exerted on it - progressive- and two sections where the layer has a negative force exerted on it - resistive.

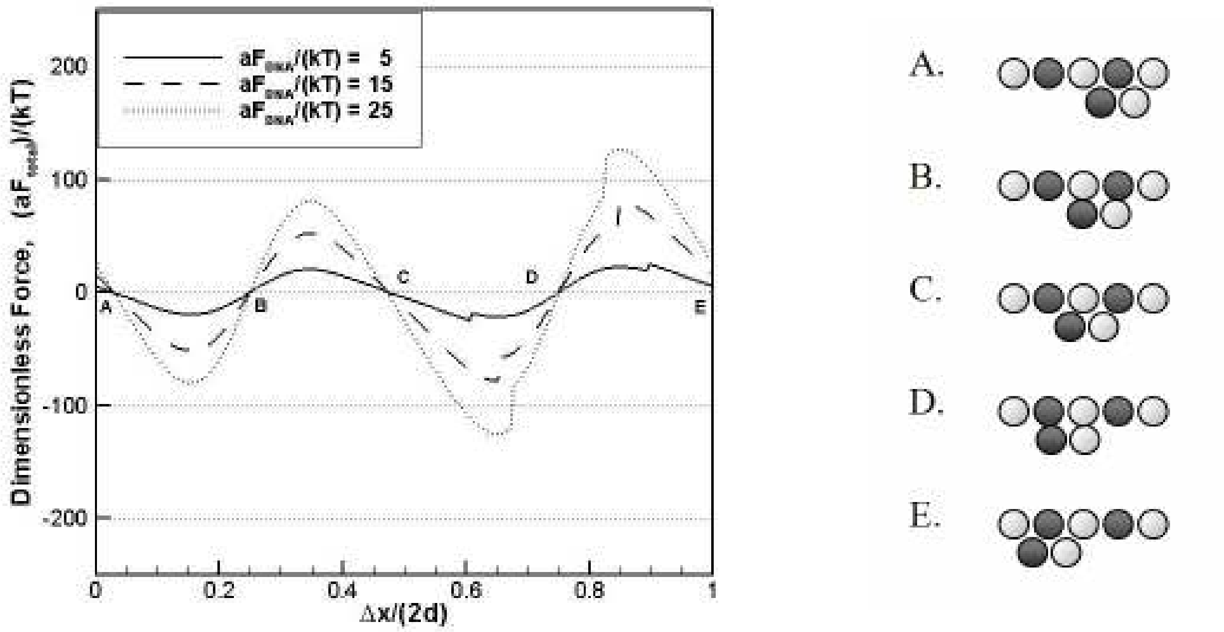

Figure 5.10: The effect of the dimensionless DNA force on the total force as a function of the displacement of a sheared layer of alternating A-type and B-type particles. As the DNA force increases so also do the relative forces. To the right are the particle orientations corresponding to the various points on the graph. $aF_o/(kT) = 923$ and $\zeta/a = 0.13$.

From the plot, the largest resistive force occurs between configurations C and D. If the shear force does not exceed this resistive force then the particles will remain fixed in a configuration somewhere between C and D. This configuration is the same configuration that was seen in the simulations; the like-type particles being perpendicular to the axis of the elongation component of the shear. The individual pairwise forces were analyzed for the two local force minima of figure 5.11; those corresponding to the two largest resistive forces. Figure 5.11 shows, qualitatively, the individual force vectors for the osmotic repulsion and the DNA attraction and their horizontal components. Figure 5.11a shows the configuration of the first resistive force. It is seen that the majority of the resistance occurs due to osmotic repulsion when the white particle comes close to passing the bottom, black particle. The attractive DNA force between the same two particles lessens the resistive force as the particles are being drawn together (the positive x-component). Figure 5.11b, on the other hand, shows the configuration of the second and largest resistive force; when the like-type particles are perpendicular to the axis of the elongation component of the shear. The large resistance to motion is still due to the osmotic repulsion of the top left particle trying to pass the bottom particle; however the horizontal component of the DNA attraction between the white and the black is now reversed and resist further motion. This reversal in the direction of the horizontal component of the DNA attraction is what results in a larger overall resistive force for this configuration. Therefore, it is the directionality of the component of the DNA force relative to the shear that determines the orientation of the linear arrays.

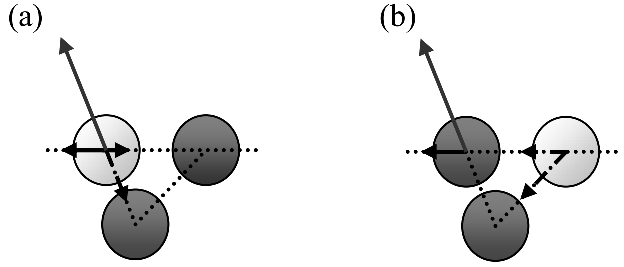

Figure 5.11: (a) The corresponding structure of the 1st force minimum given in Figure 5.10. (b) The corresponding structure of the 2nd force minimum given in Figure 5.10. Representative forces are qualitatively shown above. Dashed lines correspond to the DNA-linker force and solid lines correspond to the repulsive force. Since the distance between the layers remains fixed, only the x-component of each of the forces is considered. (b) has the stronger resistive force because it is in this orientation that the DNA attraction aids with the resistance.

A simple scaling analysis shows that the dimensional shear velocity scales as

$$U_{shear} \sim \gamma a ,$$

and the shear force scales with the inverse of the Mobility and the shear velocity:

$$F_{shear} \sim M^{-1} U_{shear} \sim (6\pi\mu a)(\gamma a) .$$

Equating the two competing forces, the dimensional DNA force with the dimensional shear force,

$$F_{DNA} \sim F_{shear} ,$$

gives the relation

$$F_{DNA} \sim 6\pi\mu a^2 \gamma ,$$

which is the condition near the order/disorder transition.

Multiplying each side by $a/(kT)$, effectively nondimensionalizing the two forces, gives the relation

$$\frac{aF_{DNA}}{kT} \sim \frac{6\pi\mu a^3\gamma}{kT},$$

or

$$\hat{F}_{DNA} \sim \hat{\gamma},$$

at the order/disorder transition in Figure 5.8 which explains why the order/disorder transition of the phase diagram can be fit with a straight line.

As the shear rate approaches zero in the phase diagram a distinct value emerges for the dimensionless DNA force ($aF_{DNA}/(kT) \sim 5$) that still forms linear arrays. Of course a shear rate exactly equal to zero would mean the shear-cycle is infinite, thus making it physically unreasonable to observe the formation of the arrays. This value of $aF_{DNA}/(kT) \sim 5$ is the minimum DNA attraction necessary for the formation of the linear arrays. A system with a DNA attraction beneath this value will never form linear arrays, irrespective of the shear rate.

Although not presented here, simulations were performed where a shear rate was applied for a given amount of time, forming the linear arrays, and then was gradually reduced to zero. We find that when the shear is stopped the linear order of the system is preserved for $aF_{DNA}/(kT)$ as small as 10. The thermal forces are not large enough to cause rearrangement of the particles, disrupting the order. Essentially, shear is a means for achieving a high degree of linear order, not a necessary condition for the preservation of order.

5.7 CONCLUSIONS

We have employed a dynamic simulation for DNA-hybridized colloidal particles confined to the surface of two fluids, quantifying the degree of linear order with the $g_2(r)$ orientational ordering parameter. We find that hydrodynamic shear offers a new and powerful tool for sampling phase space in systems where thermal sampling falls short. Specifically, we find that the addition of a hydrodynamic shear results in the formation of linear arrays. Without shear, the particles form a frustrated network showing little or no linear order. Since the pairwise interparticle potential minimum is on the order of 10s of kT we cannot expect thermal forces to do a thorough job of sampling phase space. Hydrodynamic shear is easily tunable and is capable of imparting many kT of energy to our system.

When the shear force is applied we see an ordering of A and B-type particles into linear arrays whose axis are perpendicular to the axis of the elongation component of the shear. Through our analysis we showed that the particles orient in this manner because it is this orientation that allows the DNA attraction to resist the shear, making it the most stable form. A phase diagram was then constructed identifying those systems which form linear arrays and those that did not by varying the shear rate and the dimensionless DNA force. The order/disorder transition can be fit by a straight line reinforcing our scaling argument that the dimensionless DNA force is proportional to the dimensionless shear rate. We also believe that as the shear rate approaches zero there is a distinct DNA force that will still lead to the formation of lines. In these cases, even though the shear rate is extremely small it is the number of shear cycles that the structures undergo that determines the formation of linear arrays.

Chapter 6. Summary and Conclusions

Four studies have been presented, each providing its own insight into the self-organization of 2D colloidal and nanoparticulate films. The relevant results and findings of each study are summarized below.

In a previous study Monte Carlo simulations of bidisperse hard disks were used to study the experimental observation of highly-ordered 2D arrays of bidisperse, stabilized gold nanoparticles. Our finding, however, was that kinetic limitations prevented the formation of these structures with hard disks alone. In Chapter 2, it was shown that the LS lattice forms with the addition of interparticle forces and a simple compressive force. This reveals that bidisperse lattice formation is, in fact, a dynamic process. Additionally, in every single case, RSA alone ultimately resulted in jammed, glassy microstructures. It was not possible to achieve a high enough surface coverage for stability as determined by the melting simulations.

It was evident that the LS lattice forms in large part because the particles within the lattice reside in their respective interparticle potential wells. In Chapter 3 this information was used to predict size-ratios and surface coverages for novel lattice structures, including the LS_4 and LS_6 lattices. Melting simulations were performed on each of the lattice structures determining that the LS_4 lattice was the only metastable lattice; the LS, LS_2 and LS_6 lattices all being stable lattices. These predictions are intended to guide experimentalists in their search for these exciting new structures.

A common belief is that the polydispersity of particles in nanoparticulate films disrupts the ordering of these systems. In Chapter 4, however, it was shown that polydisperse amounts of amorphous-silicon nanoparticles could, in fact, form 2D clusters exhibiting long-range orientational order even in the absence of translational order. Monte Carlo simulations were performed, which included lateral capillary forces and a simple stabilizing repulsion, resulting in structures that were strikingly similar to the experimentally observed. It was determined that these fascinating structures form as a result of lateral capillary forces, occurring during the late stages of the drying process. Essentially, as the solvent layer thickness decreases the attractions between the large particles become sufficient to induce condensation while smaller particles remain fluidized. Further evaporation induces lateral capillary forces between particles with slightly smaller diameters, forcing them to collect at the aggregate edge and so on, until all of the particles have collected at the edges of the aggregate and solvent has completely evaporated from the substrate.

Thermal energy provides an adequate means of sampling phase space when the interparticle forces are on the order of a kT of energy. Many instances, however, dictate interparticle forces that far exceed this limit. In chapter 5 it was shown that hydrodynamic forces allow a more thorough sampling of phase space than through thermal or Brownian forces alone. It was found that lines of A-type and B-type particles formed in the simulations with an imposed shear while simulations without the imposed shear formed a frustrated network with little or no linear order. An orientational distribution function, $g_2(r)$ was used to quantify the degree of linear order. A phase diagram was constructed, finding a linear dependence of the minimum DNA force necessary for line formation on the dimensionless shear rate. A force analysis was also performed on the structures showing that the lines orient perpendicular to the axis of the elongation component of the shear because it is this orientation that allows the DNA attraction to resist the shear.

Self-organization does, in fact, lead to organized structures; however, if one is interested in large areas of defect-free order in 2D this is probably not the best route. In all of the studies that were performed, it was very difficult to form crystalline structures with few defects through thermal and even hydrodynamically-assisted means alone. Certain instances, however, do not require such high degrees of order. In these cases self-assembly may suffice. When a high degree of fidelity is crucial, however, a better method appears to be that of directed self-assembly. Directing the self-assembly process with external fields (e.g. electromagnetic, hydrodynamic, lateral capillary, etc…), through functionalizations (e.g. DNA, proteins, copolymers, etc…) or through templated or patterned surfaces should lead to a greater control over the final quality of the particulate monolayer.

There is still much work to be done in understanding the process of self-organization. Though each study was thoroughly examined within its scope, the subject matter is far from exhausted. A number of proposals for further investigation are listed below.

Showing the greatest promise as a next step for the hydrodynamically-assisted self-organization of DNA-functionalized colloidal particles is the study of the effects of polydispersity on resulting microstructures. The surface density of DNA ligands on each particle should ultimately be affected by the size of the individual particle leading to new and interesting interparticle potentials. For example, the interparticle potential between a small and a large particle (S-L) should be weaker than that between a large and a large particle (L-L). In a case where hydrodynamic shear is in the right regime you should see S-L bonds being broken by the shear while the L-L bonds remain steadfast. This process of self-organization could lead to some very interesting microstructures.

Another extension for the hydrodynamic assistance problem is studying the effects of other stoichiometric ratios of A-type and B-type particles. For example, some preliminary results have shown that a 1:2 ratio of A and B particles favored the formation of LS_2 lattices; however these conditions were not intensively studied. It would be interesting to map the resulting phase diagram which might even include a transition point of favorability from the LS lattice to LS_2 lattice.

Yet another extension of the hydrodynamic assistance problem involves three or more distinct particle types with their own highly specific functionalizations. For example, one might consider a system involving A, B and C-type particles in which unlike particles exhibit a DNA attraction while like particles do not. This could also lead to some interesting results.

Outside of the hydrodynamic assistance problem are a variety of problems of substantial interest. Of great practical interest, is the problem of 2D particulate coating by drying. This problem would follow the deposition of monodisperse nanoparticles through evaporative drying with the intention of understanding the formation of the defects that arise. For example, it has been observed by Dr. Korgel's lab involving the assembly of spheres and rod-like structures into "peapod" shaped patterns. Ostensibly these structures form in a similar way as the amorphous-silicon structures of chapter 4; as a result of lateral capillary forces, which occur during the evaporation of solvent from the substrate. The handling of non-spherical particles is, of course, the next large hurdle for modelers.

To reiterate, directed assembly appears to be the preferred step towards high control over the periodic structure of particulate monolayers. Though nature uses a variety of routes for self-organization, it is this higher level of directed assembly that produces the most defect free structures among complex biological systems. Take for example the replication of the human genome. At approximately 3 billion base pairs long it is duplicated through a directed self-assembly process countless numbers of times; and with perfect fidelity. The duplication process even includes a number of proof-reading and error-detecting mechanisms ensuring the DNA copy is as true as the original. Of course this level of control over the manufacturing process is far beyond the reach of modern-day scientists, but perhaps one day, through our humble steps of today, we will develop self-assembly methods rivaling that exquisite control.

References

1. Doty, R.C., R.T. Bonnecaze, and B.A. Korgel, *Kinetic bottleneck to the self-organization of bidisperse hard disk monolayers formed by random sequential adsorption.* Physical Review E, 2002. **65**(6).
2. Gray, J.J., D.H. Klein, B.A. Korgel, and R.T. Bonnecaze, *Microstructure formation and kinetics in the random sequential adsorption of polydisperse tethered nanoparticles modeled as hard disks.* Langmuir, 2001. **17**(8): p. 2317-2328.
3. Kiely, C.J., J. Fink, M. Brust, D. Bethell, and D.J. Schiffrin, *Spontaneous ordering of bimodal ensembles of nanoscopic gold clusters.* Nature, 1998. **396**(6710): p. 444-446.
4. Kiely, C.J., J. Fink, J.G. Zheng, M. Brust, D. Bethell, and D.J. Schiffrin, *Ordered colloidal nanoalloys.* Advanced Materials, 2000. **12**(9): p. 640-+.
5. Eldridge, M.D., P.A. Madden, and D. Frenkel, *Entropy-Driven Formation of a Superlattice in a Hard-Sphere Binary Mixture.* Nature, 1993. **365**(6441): p. 35-37.
6. Brust, M. and C.J. Kiely, *Some recent advances in nanostructure preparation from gold and silver particles: a short topical review.* Colloids and Surfaces a-Physicochemical and Engineering Aspects, 2002. **202**(2-3): p. 175-186.
7. Likos, C.N. and C.L. Henley, *Complex Alloy Phases for Binary Hard-Disc Mixtures.* Philosophical Magazine B-Physics of Condensed Matter Statistical Mechanics Electronic Optical and Magnetic Properties, 1993. **68**(1): p. 85-113.
8. Saunders, A.E. and B.A. Korgel, *Second virial coefficient measurements of dilute gold nanocrystal dispersions using small-angle X-ray scattering.* Journal of Physical Chemistry B, 2004. **108**(43): p. 16732-16738.
9. Deegan, R.D., O. Bakajin, T.F. Dupont, G. Huber, S.R. Nagel, and T.A. Witten, *Capillary flow as the cause of ring stains from dried liquid drops.* Nature, 1997. **389**(6653): p. 827-829.
10. Gray, J.J., D.H. Klein, R.T. Bonnecaze, and B.A. Korgel, *Nonequilibrium phase behavior during the random sequential adsorption of tethered hard disks.* Physical Review Letters, 2000. **85**(21): p. 4430-4433.
11. Allen, M.P. and D.J. Tildesley, *Computer Simulation of Liquids*. 1987, Oxford: Oxford University Press.
12. Hunter, R.J., *Foundations of Colloid Science*. 1987, Oxford: Clarendon Press.

13. Vincent, B., J. Edwards, S. Emmett, and A. Jones, *Depletion Flocculation in Dispersions of Sterically-Stabilized Particles (Soft Spheres).* Colloids and Surfaces, 1986. **18**(2-4): p. 261-281.

14. Feder, J., *Random Sequential Adsorption.* Journal of Theoretical Biology, 1980. **87**(2): p. 237-254.

15. Pomeau, Y., *Some Asymptotic Estimates in the Random Parking Problem.* Journal of Physics a-Mathematical and General, 1980. **13**(6): p. L193-L196.

16. Swendsen, R.H., *Dynamics of Random Sequential Adsorption.* Physical Review A, 1981. **24**(1): p. 504-508.

17. Tarjus, G. and J. Talbot, *Random Sequential Adsorption of Polydisperse Mixtures - Asymptotic Kinetics and Structure.* Journal of Physics a-Mathematical and General, 1991. **24**(16): p. L913-L917.

18. Meakin, P. and R. Jullien, *Random-Sequential Adsorption of Disks of Different Sizes.* Physical Review A, 1992. **46**(4): p. 2029-2038.

19. Adamczyk, Z., B. Siwek, M. Zembala, and P. Weronski, *Influence of polydispersity on random sequential adsorption of spherical particles.* Journal of Colloid and Interface Science, 1997. **185**(1): p. 236-244.

20. Kralchevsky, P.A. and K. Nagayama, *Particles at Fluid Interfaces and Membranes: Attachment of Colloid Particles and Proteins to Interfaces and Formation of Two-Dimensional Arrays*. 2001, Amsterdam: Elsevier Science B. V.

21. Huo, F.W., A.K.R. Lytton-Jean, and C.A. Mirkin, *Asymmetric functionalization of nanoparticles based on thermally addressable DNA interconnects.* Advanced Materials, 2006. **18**(17): p. 2304-+.

22. Ohara, P.C., D.V. Leff, J.R. Heath, and W.M. Gelbart, *Crystallization of Opals from Polydisperse Nanoparticles.* Physical Review Letters, 1995. **75**(19): p. 3466-3469.

23. Sun, S.H. and C.B. Murray, *Synthesis of monodisperse cobalt nanocrystals and their assembly into magnetic superlattices (invited).* Journal of Applied Physics, 1999. **85**(8): p. 4325-4330.

24. Sun, S.H., C.B. Murray, D. Weller, L. Folks, and A. Moser, *Monodisperse FePt nanoparticles and ferromagnetic FePt nanocrystal superlattices.* Science, 2000. **287**(5460): p. 1989-1992.

25. Qi, M.H., E. Lidorikis, P.T. Rakich, S.G. Johnson, J.D. Joannopoulos, E.P. Ippen, and H.I. Smith, *A three-dimensional optical photonic crystal with designed point defects.* Nature, 2004. **429**(6991): p. 538-542.

26. John, S., *Strong Localization of Photons in Certain Disordered Dielectric Superlattices.* Physical Review Letters, 1987. **58**(23): p. 2486-2489.

27. Redl, F.X., K.S. Cho, C.B. Murray, and S. O'Brien, *Three-dimensional binary superlattices of magnetic nanocrystals and semiconductor quantum dots.* Nature, 2003. **423**(6943): p. 968-971.

28. Rabideau, B.D. and R.T. Bonnecaze, *Computational study of the self-organization of bidisperse nanoparticles.* Langmuir, 2004. **20**(21): p. 9408-9414.

29. Talapin, D.V. and C.B. Murray, *PbSe nanocrystal solids for n- and p-channel thin film field-effect transistors.* Science, 2005. **310**(5745): p. 86-89.

30. Markovich, G., C.P. Collier, S.E. Henrichs, F. Remacle, R.D. Levine, and J.R. Heath, *Architectonic quantum dot solids.* Accounts of Chemical Research, 1999. **32**(5): p. 415-423.

31. Shevchenko, E.V., D.V. Talapin, N.A. Kotov, S. O'Brien, and C.B. Murray, *Structural diversity in binary nanoparticle superlattices.* Nature, 2006. **439**(7072): p. 55-59.

32. Talapin, D.V., E.V. Shevchenko, C.B. Murray, A. Kornowski, S. Forster, and H. Weller, *CdSe and CdSe/CdS nanorod solids.* Journal of the American Chemical Society, 2004. **126**(40): p. 12984-12988.

33. Kim, F., S. Kwan, J. Akana, and P.D. Yang, *Langmuir-Blodgett nanorod assembly.* Journal of the American Chemical Society, 2001. **123**(18): p. 4360-4361.

34. Korgel, B.A. and D. Fitzmaurice, *Condensation of ordered nanocrystal thin films.* Physical Review Letters, 1998. **80**(16): p. 3531-3534.

35. Rabani, E., D.R. Reichman, P.L. Geissler, and L.E. Brus, *Drying-mediated self-assembly of nanoparticles.* Nature, 2003. **426**(6964): p. 271-274.

36. Rabideau, B.D. and R.T. Bonnecaze, *Computational predictions of stable 2D arrays of bidisperse particles.* Langmuir, 2005. **21**(23): p. 10856-10861.

37. Boudreau, L.C., J.A. Kuck, and M. Tsapatsis, *Deposition of oriented zeolite A films: in situ and secondary growth.* Journal of Membrane Science, 1999. **152**(1): p. 41-59.

38. Korgel, B.A., S. Fullam, S. Connolly, and D. Fitzmaurice, *Assembly and self-organization of silver nanocrystal superlattices: Ordered "soft spheres".* Journal of Physical Chemistry B, 1998. **102**(43): p. 8379-8388.

39. Onsager, L., *The effects of shape on the interaction of colloidal particles.* Ann. NY Acad. Sci, 1949. **51**: p. 627-659.

40. Kosterlitz, J.M. and D.J. Thouless, *Ordering, metastability and phase transitions in two-dimensional systems.* Journal of Physics C: Solid State Physics, 1973. **6**(7): p. 1181-1203.

41. Halperin, B.I. and D.R. Nelson, *Theory of 2-Dimensional Melting.* Physical Review Letters, 1978. **41**(2): p. 121-124.

42. Young, A.P., *Melting and the Vector Coulomb Gas in 2 Dimensions.* Physical Review B, 1979. **19**(4): p. 1855-1866.

43. Pell, L.E., A.D. Schricker, F.V. Mikulec, and B.A. Korgel, *Synthesis of amorphous silicon colloids by trisilane thermolysis in high temperature supercritical solvents.* Langmuir, 2004. **20**(16): p. 6546-6548.

44. Strandburg, K.J., *Bond-orientational order in condensed matter systems. Partially ordered systems.* 1992, New York: Springer-Verlag.

45. Weber, H., D. Marx, and K. Binder, *Melting Transition in 2 Dimensions - a Finite-Size-Scaling Analysis of Bond-Orientational Order in Hard Disks.* Physical Review B, 1995. **51**(20): p. 14636-14651.

46. Antonietti, M., J. Hartmann, M. Neese, and U. Seifert, *Highly ordered size-dispersive packings of polydisperse microgel spheres.* Langmuir, 2000. **16**(20): p. 7634-7639.

47. Yamaki, M., J. Higo, and K. Nagayama, *Size-Dependent Separation of Colloidal Particles in 2-Dimensional Convective Self-Assembly.* Langmuir, 1995. **11**(8): p. 2975-2978.

48. Kralchevsky, P.A. and K. Nagayama, *Capillary Forces between Colloidal Particles.* Langmuir, 1994. **10**(1): p. 23-36.

49. Nicolson, M.M., *The interaction between floating particles.* Proeedings of the Cambridge Philosophical Society, 1949. **45**: p. 288-295.

50. Chan, D.Y.C., J.D. Henry, and L.R. White, *The Interaction of Colloidal Particles Collected at Fluid Interfaces.* Journal of Colloid and Interface Science, 1981. **79**(2): p. 410-418.

51. Kralchevsky, P.A., N.D. Denkov, V.N. Paunov, O.D. Velev, I.B. Ivanov, H. Yoshimura, and K. Nagayama, *Formation of 2-Dimensional Colloid Crystals in Liquid-Films under the Action of Capillary Forces.* Journal of Physics-Condensed Matter, 1994. **6**: p. A395-A402.

52. Israelachvili, J.N., *Intermolecular and surface forces*. 1991, London: Academic Press.

53. Joannopoulos, J.D., P.R. Villeneuve, and S.H. Fan, *Photonic crystals: Putting a new twist on light.* Nature, 1997. **386**(6621): p. 143-149.

54. Breslauer, K.J., R. Frank, H. Blocker, and L.A. Marky, *Predicting DNA Duplex Stability from the Base Sequence.* Proceedings of the National Academy of Sciences of the United States of America, 1986. **83**(11): p. 3746-3750.

55. Biancaniello, P.L. and J.C. Crocker, *Line optical tweezers instrument for measuring nanoscale interactions and kinetics.* Review of Scientific Instruments, 2006. **77**(11).

56. Kim, A.J., P.L. Biancaniello, and J.C. Crocker, *Engineering DNA-mediated colloidal crystallization.* Langmuir, 2006. **22**(5): p. 1991-2001.

57. Milam, V.T., A.L. Hiddessen, J.C. Crocker, D.J. Graves, and D.A. Hammer, *DNA-driven assembly of bidisperse, micron-sized colloids.* Langmuir, 2003. **19**(24): p. 10317-10323.

58. Rogers, P.H., E. Michel, C.A. Bauer, S. Vanderet, D. Hansen, B.K. Roberts, A. Calvez, J.B. Crews, K.O. Lau, A. Wood, D.J. Pine, and P.V. Schwartz, *Selective, controllable, and reversible aggregation of polystyrene latex microspheres via DNA hybridization.* Langmuir, 2005. **21**(12): p. 5562-5569.

59. Valignat, M.P., O. Theodoly, J.C. Crocker, W.B. Russel, and P.M. Chaikin, *Reversible self-assembly and directed assembly of DNA-linked micrometer-sized colloids.* Proceedings of the National Academy of Sciences of the United States of America, 2005. **102**(12): p. 4225-4229.

60. Mirkin, C.A., R.L. Letsinger, R.C. Mucic, and J.J. Storhoff, *A DNA-based method for rationally assembling nanoparticles into macroscopic materials.* Nature, 1996. **382**(6592): p. 607-609.

61. Tkachenko, A.V., *Morphological diversity of DNA-colloidal self-assembly.* Physical Review Letters, 2002. **89**(14).

62. Mucic, R.C., J.J. Storhoff, C.A. Mirkin, and R.L. Letsinger, *DNA-directed synthesis of binary nanoparticle network materials.* Journal of the American Chemical Society, 1998. **120**(48): p. 12674-12675.

63. Grassia, P.S., E.J. Hinch, and L.C. Nitsche, *Computer-Simulations of Brownian-Motion of Complex-Systems.* Journal of Fluid Mechanics, 1995. **282**: p. 373-403.

64. Lees, A.W. and S.F. Edwards, *The computer study of transport processes under extreme conditions.* Journal of Physics C: Solid State Physics, 1972. **5**(15): p. 1921-1928.

65. Li, P.T.X., C. Bustamante, and I. Tinoco, *Unusual mechanical stability of a minimal RNA kissing complex.* Proceedings of the National Academy of Sciences of the United States of America, 2006. **103**(43): p. 15847-15852.

Vita

Brooks Douglas Rabideau was born in Denver, Colorado, on March 3, 1979 to Dana and Clara Rabideau. He graduated from Southside High School in Fort Smith, Arkansas in June 1997. That fall he entered Northwestern University in Evanston, Illinois and received a Bachelor of Science degree in Chemical Engineering in May 2001. He entered the graduate school at the University of Texas at Austin in June 2001, pursuing a doctoral degree in Chemical Engineering. After graduation, Brooks is assuming a post-doctoral position with the University of Eastern Paris in Paris, France.

Permanent address: 1621 S. Albert Pike, Fort Smith, AR 72903

This dissertation was typed by Brooks D. Rabideau.